

Response of rate-and-state seismogenic faults to harmonic shear-stress perturbations

Thomas J. Ader,^{1,2} Nadia Lapusta,^{1,3} Jean-Philippe Avouac¹ and Jean-Paul Ampuero¹

¹Division of Geological and Planetary Sciences, California Institute of Technology, Pasadena, CA 91125, USA. E-mail: ader@caltech.edu

²Laboratoire de Géologie, Ecole Normale Supérieure, CNRS, 24 rue Lhomond, F-75004 Paris, France

³Division of Engineering and Applied Science, California Institute of Technology, Pasadena, CA 91125, USA

Accepted 2014 April 14. Received 2014 April 10; in original form 2013 September 20

SUMMARY

Field and laboratory observations show that seismicity has non-trivial period-dependent response to periodic stress perturbations. In Nepal, seismicity shows significant variations in response to annual monsoon-induced stress variations but not to semidiurnal tidal stresses of the same magnitude. Such period dependence cannot be explained by the Coulomb failure model and spring-slider rate-and-state model (SRM). Here, we study seismicity response to periodic stress perturbations in a 2-D continuum model of a rate-and-state fault (that is, a finite rate-and-state fault). We find that the resulting seismicity indeed exhibits nearly periodic variations. Their amplitude is maximum at a certain period, T_a , and decreases with smaller and larger periods to the SRM predictions, remaining much larger than the SRM predictions for a wide range of periods around T_a . We attribute the higher sensitivity of finite faults to their finite nucleation zones which vary in space and have a different slip-velocity evolution than that of the SRM. At periods $T \gg T_a$ and $T \ll T_a$, the seismicity-rate variations are in phase with the stress-rate and stress variations, respectively, consistent with the SRM, although a gradual phase shift appears as T increases towards T_a . Based on the similarities with the SRM and our simulations, we propose a semi-analytical expression for T_a . Plausible sets of model parameters make T_a equal to 1 yr, potentially explaining Nepal observations and constraining the fault properties. Our finite-fault findings indicate that $a\sigma$, where a is a rate-and-state parameter and σ is the effective normal stress, can be severely underestimated based on the SRM.

Key words: Seismic cycle; Earthquake dynamics; Seismicity and tectonics.

1 INTRODUCTION

How a seismogenic fault responds to an applied stress history remains a fundamental question in seismotectonics. One of the main obstacles to addressing this question is the limited range of configurations of stress variations and the resulting seismicity rate that can be constrained from observations of natural fault systems. The response of seismicity to either a constantly increasing stress, a stress step (e.g. Gross & Kisslinger 1997; Gross & Bürgmann 1998; Toda *et al.* 1998, 2012), or a periodically varying stress (e.g. Heki 2003; Cochran *et al.* 2004; Bollinger *et al.* 2007; Christiansen *et al.* 2007; Bettinelli *et al.* 2008; Ader & Avouac 2013) are the most common configurations occurring in nature. Fortunately, these three configurations actually constitute the standard approach to establishing and characterizing the transfer function of a linear system, which is fully determined by its ramp, step, and harmonic responses. In principle, it might thus be possible to infer the transfer function relating seismicity to stress from the response of seismogenic faults to such stress perturbations (Fig. 1). Seismogenic faults are non-linear systems since friction is inherently non-linear. This study

contributes to assessing this transfer function through numerical simulations of fault dynamics subjected to quasi-static stress perturbations. Earthquakes can also be triggered by seismic waves (e.g. Hill 1993; Gombert *et al.* 2003; Felzer & Brodsky 2006) as well as pore fluid motion and induced variations in fault strength (e.g. Nur & Booker 1972; Bosl & Nur 2002; Hainzl & Fischer 2002; Saar & Manga 2003; Hainzl *et al.* 2006; Cappa *et al.* 2009; Dahm *et al.* 2010), but these mechanisms are beyond the scope of this study.

The case of a simple constant loading rate on a fault is probably the most common in nature. At plate interfaces, for instance, where faults are steadily loaded by the slow motion of tectonic plates, over a time period much longer than the characteristic return period of seismic events, the stressing rate can be regarded as constant through time and results in an approximately constant seismicity rate, often called 'background' rate. Aftershock sequences following large events are the most frequent type of deviation from this constant background seismicity. Under the premise that aftershocks are statically triggered by the static stress change caused by a main shock, their evolution can be seen as the response of the seismicity to a step-like function in stress. This evolution is characterized by

a sudden jump of the seismicity rate immediately after the main shock, followed by a gradual decay of the seismicity rate with time back to its pre main shock level, according to the Omori law (see Utsu *et al.* 2005, for a recent review). The time evolution, amplitude and other characteristics of aftershock sequences have thus been broadly studied, in order to find a way to measure fault properties (e.g. Gross & Kisslinger 1997; Gross & Bürgmann 1998; Toda *et al.* 1998, 2012).

Another case that arises in nature is that of a periodic loading, generally either due to tides (e.g. Wilcock 2001; Tanaka *et al.* 2002; Cochran *et al.* 2004), or seasonal loading due to the local hydrological cycle (e.g. Heki 2003; Christiansen *et al.* 2005, 2007; Bollinger *et al.* 2007; Bettinelli *et al.* 2008). Correlation of seismicity with tides has been reported, for example, by Cochran *et al.* (2004), who showed a correlation between the occurrence of shallow thrust earthquakes and the occurrence of the strongest tides for $M > 5.5$ events from the global Harvard centroid moment tensor (CMT) catalogue. Seasonal variations of seismicity following seasonal variations of stress loading on a fault have been reported at different locations. Heki (2003) pointed out possible variations of seismicity in Japan, due to annual variations of snow load. Snow unloading coupled to groundwater recharge was also reported to induce seasonal variations of seismicity in western U.S. volcanic centres (Christiansen *et al.* 2005), by modifying the stress on the fault by about 5 kPa. There are also examples of seismicity variations due to surface load variations associated with the hydrological cycle. Along the San Andreas fault, Christiansen *et al.* (2007) observed that hydrologically induced stress perturbations of ~ 2 kPa might be sufficient to affect seismicity, either due to a direct surface load variations or to pore-pressure variations. In the Nepal Himalaya, hydrologically induced variations of the Coulomb stress of 2–4 kPa appear to produce seasonal variations of the seismicity rate of ~ 40 per cent, in phase with the variations of stress rate on the fault (Bollinger *et al.* 2007; Bettinelli *et al.* 2008; Ader & Avouac 2013). Yet, no seismicity-rate variations have been observed at tidal periods, indicating that if

such variations exist, they have amplitude changes of less than 18 per cent (Ader & Avouac 2013), although the variations of stress due to solid-Earth tides are of similar amplitude as those caused by the hydrological loading (Bettinelli *et al.* 2008). This findings indicate a period-dependent response of the Nepalese seismicity, with less sensitivity at tidal periods than to the annually occurring monsoon.

Such a period-dependent response of faults has been observed in various laboratory experiments, where frictional interfaces are subjected to harmonic stress variations (Lockner & Beeler 1999; Beeler & Lockner 2003; Savage & Marone 2007, 2008). At periods larger than a critical period, the rate of stick-slip events (assumed equivalent to a seismicity rate) obtained in the experiments appears to be directly proportional to the rate of harmonically varying stress. In such a regime, the amplitude of the seismicity-rate variations is inversely proportional to the perturbation period. At shorter periods, lab experiments by Lockner & Beeler (1999) and Beeler & Lockner (2003) suggested a slightly period-dependent response, with the correlation between the timing of events and the stress perturbation increasing with the perturbation period. This period-dependent response at shorter periods could explain the observations in Nepal.

It is important to establish which fault physics, represented by the grey box in Fig. 1, is consistent with the observed period-dependent response in Nepal. The mechanisms acting on faults seem to be well described by the formalism of rate-and-state friction (Dieterich 1978, 1979a,b; Ruina 1983), where the friction between two rock surfaces or within a granular rock layer depends on the relative slip velocity and a state variable evolving with time. The rate-and-state friction laws have been established in order to reproduce the observations that the onset of frictional sliding in lab experiments is a time-dependent process, and introduce a time-dependent failure mechanism for the generation of earthquakes. The laws have been used to model and reproduce a number of earthquake-source observations (Dieterich 1987, 2007).

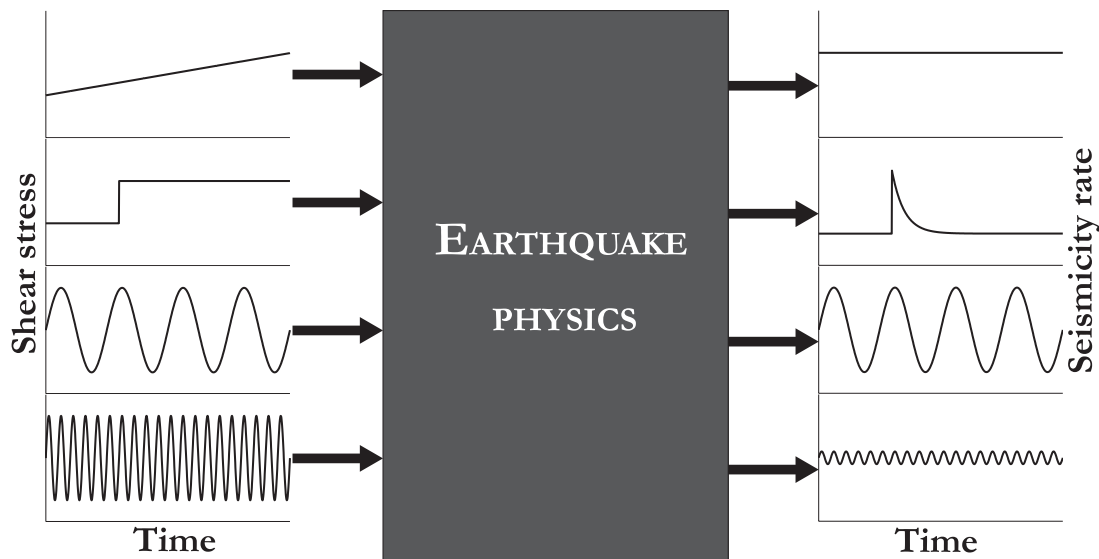


Figure 1. Cartoon presenting the challenge underlying today’s knowledge of earthquake physics. The earthquake physics, that would predict how a fault reacts to an imposed stress history, remains somewhat of a grey box. Few stress-loading configurations arise naturally and some have been tested in the lab, although lab experiments may not capture the full behaviour of natural faults. Most natural faults are loaded at near-constant stress rates, which results in constant seismicity rates. A population of faults undergoing a stress step (due to a main shock) sees its seismicity rate suddenly increase and gradually decay back to the initial seismicity rate, following the Omori law. Seismicity in Nepal gives us the response of seismicity to periodic stresses of comparable amplitudes but different periods, and suggests a larger seismic response to a larger perturbing period, something that cannot be explained by the current seismicity-rate models.

Using this formalism and modeling the earthquake-generation process on faults with a simple one-degree-of-freedom spring-and-slider system obeying rate-and-state friction laws, Dieterich (1994) proposed an analytical expression linking the stress history on a fault to the expected resulting seismicity rate. Some of the observations described earlier can be explained by the predictions of this spring-slider rate-and-state model (SRM). The Omori law for the decay of aftershocks rate with time is well reproduced by the SRM (Dieterich 1994), although it requires a near-lithostatic pore pressure where aftershocks nucleate in order to quantitatively explain the typical duration of aftershock sequences (e.g. Gross & Kisslinger 1997; Gross & Bürgmann 1998; Toda *et al.* 1998, 2012). In the case of harmonic stress perturbations, the SRM explains the phase shift between the stress perturbations and the resulting seismicity-rate variations (e.g. Beeler & Lockner 2003). Applied to the observations in Nepal, the SRM requires a near-lithostatic pore pressure in the seismogenic zone in order to explain the amplitude of the correlation between the seismicity rate and the monsoon-induced variations of stress (Bettinelli *et al.* 2008). This can be problematic, since near-lithostatic pore pressures require specific fault properties for the nucleation sizes to remain consistent with the occurrence of the smallest earthquakes recorded as well as result in effective normal stresses orders of magnitude below the values reported from afterslip studies in various tectonic contexts (Hearn *et al.* 2002; Miyazaki *et al.* 2004; Perfettini & Avouac 2004, 2007; Hsu *et al.* 2006, 2009a,b; Barbot *et al.* 2009; Fukuda *et al.* 2009), as highlighted in a study of non-volcanic tremors (Ader *et al.* 2012). Moreover, the SRM does not explain the period-dependent response of the seismicity to harmonic stress perturbations at shorter periods as observed in lab experiments (Lockner & Beeler 1999; Beeler & Lockner 2003) and in Nepal (Bettinelli *et al.* 2008; Ader & Avouac 2013).

In this study, we therefore drop the spring-slider approximation and study the response of a 2-D elastodynamic model with a 1-D seismogenic fault obeying rate-and-state friction laws to harmonically varying stress perturbations of different periods. In other words, we investigate the harmonic response of a seismogenic finite fault. To do so, we conduct fully dynamic simulations of earthquake sequences (Lapusta *et al.* 2000; Lapusta & Rice 2003; Lapusta & Liu 2009; Noda & Lapusta 2010) on a seismogenic patch of finite size surrounded by creeping areas, and undergoing stress perturbation. The model considers only one fault with multiple seismic events but we assume that the statistic we get out of these simulations is representative of the statistics we would obtain assuming a population of faults with random initial stress conditions. In Nepal, most of the earthquakes occur on a population of faults distributed in a volume around the downdip edge of the locked portion of the MHT, between 5 and 15 km of depth (Cattin & Avouac 2000). This is an area where both seismic and aseismic slip can occur and interplay (whether on the MHT or in the surrounding medium). Our model incorporates that ingredient, but actually, the creeping area surrounding the seismic patch is also a convenient way to bound the seismic ruptures. In reality, seismic ruptures could in fact be bounded by geometric effects or by zones of low stress shed by previous earthquakes. The motivation for studying the response of a finite fault comes from the study of Kaneko & Lapusta (2008) which showed that finite faults have different responses to shear stress than spring-slider models. This study mostly focuses on the response of such a finite fault to harmonic perturbations, but we also present some results of the step response of the finite fault.

In the following, we start by briefly reviewing, in Sections 2 and 3, the expected seismicity-rate response to the step-like and harmonic

stress perturbations of a one-degree-of-freedom fault in both the Coulomb failure model (CFM) and the SRM. We then present the finite-fault simulations that constitute the core of this study, by first describing the methodology in Section 4 and then the frequency response of finite faults in Section 5. Section 6 introduces results of the step response, highlighting properties of the finite fault revealed by the frequency response as well as illustrating the general non-linearity of the response. We discuss our interpretation of the results in Section 7 and conclude in Section 8.

2 RESPONSE OF SEISMICITY IN THE CFM

The CFM is probably the simplest way to conceptualize the relation between stressing and earthquake occurrence on a fault. It assumes that whenever the Coulomb stress $S = \tau - \mu\sigma_{\text{eff}}$, where μ is the friction coefficient, τ the shear stress and σ_{eff} the effective normal stress (i.e. the normal stress reduced by the pore pressure), reaches a threshold value called the Coulomb failure stress (CFS), the fault produces an earthquake and the stress on the fault drops to a lower value. Assuming, in addition, a population of faults on which the pre-stresses are uniformly distributed up to the CFS, the observed seismicity rate $R(t)$ is therefore proportional to the Coulomb stress rate $\dot{S}(t)$, and thus to the shear-stress rate $\dot{\tau}(t)$ when the normal stress is kept constant. Since the seismicity rate cannot have negative values, this relation of direct proportionality remains true only as long as the Coulomb stress keeps increasing. If it starts decreasing, there will be no earthquake until it grows back to a value equal to its last maximum. Denoting by $S_f(t)$ the non-decreasing envelope of the Coulomb stress $S(t)$ [see Fig. A1(a) for a representation of the corresponding functions $\tau(t)$ and $\tau_f(t)$], the seismicity rate $R(t)$ in the CFM can be written as (Appendix A):

$$R(t) \propto \dot{S}_f(t). \quad (1)$$

In the case of a step-like change of stress on the fault, eq. (1) leads to a simple impulse change of the seismicity rate, and therefore, this model does not reproduce the Omori law for the decay of aftershocks with time.

The case of the response to a harmonic stress perturbation is more interesting. The seismicity rate in the CFM is proportional to the stress rate as reported for the seasonal variations of seismicity in Nepal (Bettinelli *et al.* 2008) and for the results of laboratory experiments at larger perturbing periods (Lockner & Beeler 1999; Beeler & Lockner 2003; Savage & Marone 2007, 2008). Given a background loading rate of shear stress $\dot{\tau}_a$, superimposing harmonic variations of shear-stress of amplitude $\Delta\tau$ might cause the resulting shear stress to periodically decrease, if the period T of the perturbation is short enough (Fig. A1a). We show in Appendix A that, depending whether the period T of the perturbation is greater or smaller than the critical period $T_c = 2\pi\Delta\tau/\dot{\tau}_a$, the relative amplitude of the variations of seismicity rate is different and given by:

$$\frac{\Delta R}{r} = \frac{T_c}{T} \quad \text{when } T \geq T_c, \quad (2)$$

and

$$\frac{\Delta R}{r} = 2\sqrt{\pi}\sqrt{\frac{T_c}{T}} \quad \text{when } T \ll T_c. \quad (3)$$

Eqs (2) and (3) suggest that, at all periods, the amplitude of the seismicity response increases as the period decreases, as confirmed by our numerical computation (Fig. 2). This property would imply

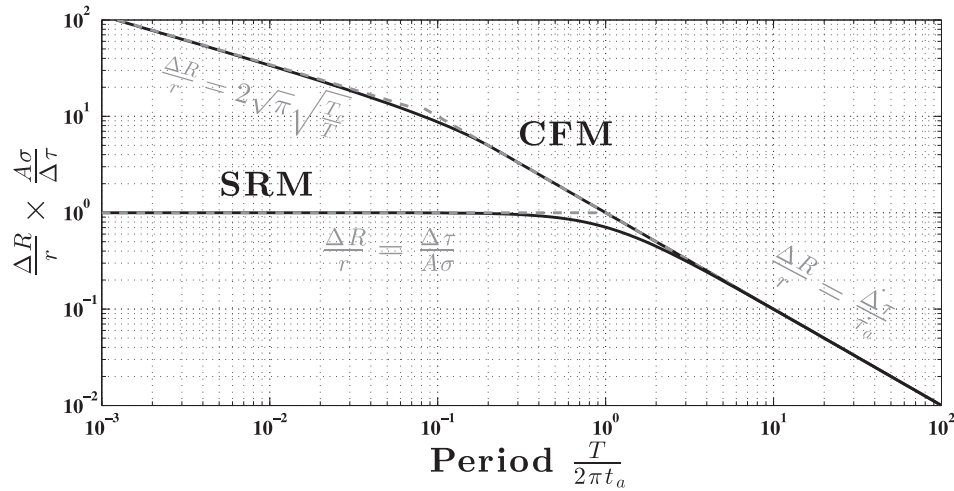


Figure 2. The amplitude of seismicity-rate variations for different periods of harmonic variations in shear stress, according to the Coulomb failure model (CFM) and spring-slider rate-and-state model (SRM). The black curves represent the numerical solution to the exact equations while the grey dashed lines represent the asymptotic behaviour, with corresponding equations indicated on the plot, and derived in the appendices.

a greater response of the seismicity to the semidiurnal tidal loading than to the annual forcing, in contradiction with the observations in Nepal discussed in Section 1. This property is also incompatible with the results of lab experiments at shorter perturbing periods by Lockner & Beeler (1999) and Beeler & Lockner (2003). The predicted amplitude of the variations of seismicity rate $\Delta R/r$ in response to a harmonic perturbation of shear stress of amplitude $\Delta\tau$ by the CFM is plotted in Fig. 2 as a function of the perturbing period T .

3 RESPONSE OF SEISMICITY IN THE SPRING-SLIDER RATE-AND-STATE MODEL (SRM)

The major issue with the CFM is that it does not contain any intrinsic time delay for the earthquake-nucleation process, that could reproduce the gradual decay of the aftershock rate following a main shock. Dieterich (1994) proposed an alternative model of the seismicity rate on a fault based on a one degree of freedom spring-and-slider system following rate-and-state friction laws.

In the rate-and-state formalism, the evolution of the friction coefficient μ between two rock surfaces or in gouge layers, or below the slider in the case of the SRM, logarithmically depends on the slip rate V and a state variable θ (Dieterich 1978, 1979a,b; Ruina 1983):

$$\mu = \mu^* + a \ln \frac{V}{V^*} + b \ln \frac{\theta V^*}{D_c}, \quad (4)$$

where μ^* is the reference friction coefficient corresponding to the reference slip velocity V^* , D_c is the characteristic slip for state evolution (e.g. Dieterich 1978, 1979a,b; Ruina 1983; Rice & Ruina 1983; Dieterich & Kilgore 1994), and $a > 0$ and $b > 0$ are rate-and-state constitutive fault parameters with $a - b < 0$ so that the system has a rate-weakening steady-state rheology. The state variable θ can be interpreted as the average age of the population of frictional contacts. Several state-evolution laws have been proposed; in this study, we adopt the ‘aging law’ (e.g. Marone 1998):

$$\frac{d\theta}{dt} = 1 - \frac{V\theta}{D_c}. \quad (5)$$

Note that the state variable evolves with time even if there is no relative motion ($V = 0$), reflecting experimental observations of friction increasing with the hold time.

In order to derive the seismicity rate on a population of faults undergoing a time-varying stress, the SRM of Dieterich (1994) makes a few assumptions. The model assumes that the times to failure of the faults are uniformly distributed in the case of a constant stress rate, and that variations of stress on the faults simply modify the time to failure. Besides, it is assumed that, during nucleation, the velocity on the fault is large enough so that $V\theta/D_c \gg 1$, thus reducing eq. (5) to $d\theta/dt = -V\theta/D_c$. The relations obtained are reviewed in Appendix B for the case of a constant normal stress. For a stress step mimicking a sudden stress change produced by a nearby main shock, the SRM’s relations successfully reproduce the Omori law for the time decay of aftershocks (eq. 12 from Dieterich 1994). The cumulative number of events following a stress step at time $t = 0$ is given by:

$$N(t) = rt + rt_a \ln[e^{\Delta\tau/a\sigma} + (1 - e^{\Delta\tau/a\sigma})e^{-t/t_a}] \mathcal{H}(t), \quad (6)$$

where

$$t_a = a\sigma/\dot{\tau}_a \quad (7)$$

is the characteristic relaxation time of the seismicity rate following a stress step (i.e. the characteristic duration of an aftershock sequence), and $\mathcal{H}(t)$ is the Heavyside function, that is, $\mathcal{H}(t) = 0$ for $t < 0$ and $\mathcal{H}(t) = 1$ for $t \geq 0$.

This model is able to link the parameters of the rate-and-state formalism and the empirical Omori’s law for the time decay of aftershocks. It has therefore fostered numerous studies inferring fault properties from observations of aftershock-sequence decays (e.g. Gross & Kisslinger 1997; Gross & Bürgmann 1998; Toda *et al.* 1998, 2012). With the estimates of the stress-step amplitude $\Delta\tau$ and the secular stress rate $\dot{\tau}_a$ on the fault, fitting eq. (6) to the observed cumulative number of events in the aftershock sequence yields estimates of the product $a\sigma$. The fault parameter a has been measured in laboratory experiments (Dieterich 1994, found 0.005–0.012) and, assuming that these laboratory-derived values can be applied to real faults, $a\sigma$ leads to estimates of the effective normal stress at the depth of the aftershock sequence.

This exercise has been performed on numerous aftershock sequences, systematically leading to effective normal stresses one to several orders of magnitude below the lithostatic pressure at studied depths. Using the temporal evolution of the 1992 Landers event aftershocks, for instance, Gross & Kisslinger (1997) constrained $a\sigma$ to be between 23 and 47 kPa. Following the same procedure for the 1989 Loma Prieta earthquake, Gross & Bürgmann (1998) estimated $a\sigma = 11\text{--}330$ kPa, depending on the value of t_a in the fit. In Japan, Toda *et al.* (1998) computed $a\sigma = 35$ kPa for the time decay of the aftershocks of the 1995 Kobe event, and Toda *et al.* (2012) reported $a\sigma = 10$ kPa for the Joshua Tree and Landers earthquakes. Noting that an effective normal stress equal to the hundreds of MPa of overburden pressure at seismogenic depths would lead to values of a much less than the range of the laboratory-derived values (Dieterich 1994), these studies thus concluded that the prevailing effective normal stress should be of the order of a few MPa, that is, two orders of magnitude below the lithostatic value. To explain this difference, they resorted to near-lithostatic pore pressures at seismogenic depths.

Regarding the response of seismicity to harmonic stress perturbations, one can conceptually understand how the time-dependent failure mechanism introduced by the rate-and-state laws in the SRM might be able to dampen the frequency response at shorter periods: if the nucleation time of events t_a is much larger than the stress-perturbation period T , the stress variations seen by the seismicity are smoothed out, and the amplitude of the seismicity response is reduced. Conversely, in the opposite case where the nucleation time t_a is much smaller than the stress-perturbation period T , the existence of a nucleation time will simply introduce a phase shift $\Phi \sim 2\pi t_a/T$ between the stress rate and the seismicity rate, rapidly negligible with increasing T , but should not produce a response much different from the one predicted by the CFM. The complete derivation of the harmonic response for the SRM is detailed in Appendix B. As has been noted in previous studies (e.g. Lockner & Beeler 1999; Beeler & Lockner 2003) and described before, this model indeed predicts two different behaviours of the seismicity response (Fig. 2), depending on whether the period of the perturbation T is larger or smaller than the characteristic period T_a , defined as

$$T_a = 2\pi t_a = 2\pi \frac{a\sigma}{\dot{\tau}_a}. \quad (8)$$

As expected, the critical period T_a is directly related to the characteristic relaxation time t_a .

For perturbation periods $T \gg T_a$, the seismicity responds in a Coulomb failure fashion. The seismicity rate is directly proportional to the stress rate as long as it remains positive, otherwise, a seismicity quiescence is observed, exactly following the predictions of the CFM (see eqs B14 and B15 in the Appendix). In the case of perturbations of period $T \ll T_a$, the response of the seismicity is lower than the predictions of the CFM, as expected. The amplitude of the seismicity-rate variations actually becomes independent of the period, and the seismicity rate in response to a shear-stress perturbation $\tau(t) = \dot{\tau}_a t + \Delta\tau \sin \omega t$ can be written as (eq. B13 in the Appendix):

$$R(t) \propto \exp\left(\frac{\Delta\tau}{a\sigma} \sin \omega t\right). \quad (9)$$

In the case $\Delta\tau \ll a\sigma$, the relative amplitude of the seismicity rate around its unperturbed value is simply $\Delta R/r = \Delta\tau/a\sigma$ (eq. B7). This small-perturbation configuration is the one considered later in the finite-fault simulations, in order to avoid introducing any extra

source of non-linearity. Like for aftershock-rate predictions, these simple expressions have enabled studies to determine values of the product $a\sigma$ from real cases of variations of seismicity. Looking at triggering of earthquakes by tides worldwide, Cochran *et al.* (2004) fitted the amplitude of induced variations of seismicity with the SRM and provided a range of values for $a\sigma$ between 48 and 110 kPa, with a best fit of 64 kPa, values of the same order of magnitude as the ones inferred from the study of aftershock sequences. Based on the results of the SRM, Bettinelli *et al.* (2008) reported that for the Nepalese seismicity to be able to respond to seasonal variations of surface water load, extremely low values of $a\sigma$ (between 3 and 8 kPa) were required. These results would thus also suggest extremely low effective normal stresses at the seismogenic depth of the faults, at least at places where aftershocks nucleate.

The SRM reproduces, at least qualitatively, the usually observed time decay of aftershocks rates, but an issue remains for the frequency response. Even though the response of the seismicity at short periods is dampened compared to what the CFM would predict, the amplitude of the response remains constant as the period gets shorter. Therefore, the SRM cannot explain the observations in Nepal and the results of lab experiments by Lockner & Beeler (1999) and Beeler & Lockner (2003). Besides, it would require a near-lithostatic pore pressure, that is, extremely low normal stresses at seismogenic depths in order to quantitatively explain both aftershock sequences and response to periodic perturbations. As mentioned earlier, low effective normal stresses might be a problem for the nucleation of the smallest recorded events, and they are not observed in afterslip studies. However, the one-degree-of-freedom SRM model has a different response than a fault with finite dimension (Kaneko & Lapusta 2008).

We thus investigate whether a rate-and-state fault is able to reproduce the results observed for the step and harmonic responses of seismicity, by setting aside the one-degree-of-freedom spring-slider approximation and examining what would be the behaviour of a finite fault with rate-and-state friction under such stress perturbations.

4 MODELING A FINITE RATE-AND-STATE FAULT

We study the behaviour of a 1-D fault embedded into a 2-D elastodynamic continuum, as schematically represented in Fig. 3. The fault is infinite in one direction and consists of a potentially seismogenic rate-weakening patch ($a - b < 0$), surrounded by rate-strengthening areas ($a - b > 0$). The fault is 3 km long and, unless stated otherwise, discretized into 6000 cells of 0.5 m each. Unless indicated otherwise, the seismogenic patch is 500 m long. The evolution of the slip on this finite rate-and-state fault is simulated using the Boundary Integral CYCLE of Earthquakes (BICYCLE) approach (Lapusta *et al.* 2000; Lapusta & Rice 2003; Lapusta & Liu 2009; Noda & Lapusta 2010). Several thousands of earthquakes are simulated in order to have a statistically significant number of events. The fault is loaded at a constant slip velocity $V_{pl} = 1 \text{ cm yr}^{-1}$ (unless indicated otherwise) on both sides, and the rate-and-state parameters are: $a = 0.008$ on the entire fault, $b = 0.012$ on the seismogenic patch and 0.004 in the creeping zone, $D_c = 5 \text{ }\mu\text{m}$, and $\mu^* = 0.6$ at slip rate $V^* = 10^{-6} \text{ m s}^{-1}$. The medium has a shear modulus of $G = 30 \text{ GPa}$ and, unless noted otherwise, $\sigma = 5 \text{ MPa}$. In fully dynamic simulations of 2-D antiplane earthquakes sequences, resolving the cohesive zone size Λ_0 with 3–5 spatial cells is a more stringent requirement for the aging formulation of rate-and-state

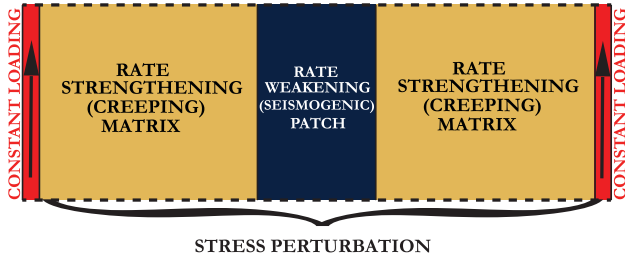


Figure 3. Schematics of the finite fault used in the numerical simulations. The fault is infinite in one direction, and consists of one rate-weakening (seismogenic) patch embedded within a rate-strengthening medium. The whole fault is loaded on both sides at a constant slip velocity. The stress perturbation (either a step function or a harmonic perturbation) is applied over the entire fault. Unless otherwise indicated, the fault has a length of 3 km, and the seismogenic patch at the center is 500 m long. The normal stress is held constant at $\sigma = 5$ MPa. The rate-and-state fault parameters are: $a = 0.008$ over the entire fault, $b = 0.012$ in the seismogenic patch (so that $a - b < 0$) and $b = 0.004$ in the rate-strengthening region (so that $a - b > 0$), $D_c = 5$ μm , and the reference friction coefficient is $\mu^* = 0.6$ at the reference slip velocity $V^* = 10^{-6}$ m s^{-1} .

friction and typical rate-and-state parameters than resolving the nucleation size (Lapusta & Liu 2009). For a fault interface governed by rate-and-state friction laws, Λ_0 can be expressed as (Palmer & Rice 1973; Day *et al.* 2005; Lapusta & Liu 2009):

$$\Lambda_0 = \frac{GD_c}{b\sigma}. \quad (10)$$

In our case, $\Lambda_0 = 2.5$ m, which justifies our choice of 0.5 m for the cell size. Our choice of $\sigma = 5$ MPa is motivated by the small stress perturbations we would like to study and the fact that the SRM predicts an amplitude not greater than $\Delta\tau/a\sigma$ for the response of the seismicity rate to a stress perturbation of amplitude $\Delta\tau$. In order to look at stress perturbations of the order of 3 kPa, as has been estimated for the monsoon-induced and tidal stresses in Nepal, we settle for the largest normal stress able to bring out a response of the seismicity large enough to be detected in the SRM, and we study the dependence of the response on the effective normal stress.

Fig. 4(a) shows the natural evolution of slip along the fault over about 2 yr, without any exterior stress perturbation. In order to represent both the interseismic and coseismic slip in Fig. 4(a), the slip is plotted every 0.01 yr if the fault is in the interseismic regime and every 0.02 seconds if it is in the coseismic regime. We consider that a seismic event is occurring on the fault when the maximum velocity on the fault is greater than 1 cm s^{-1} , which is many orders of magnitude greater than the loading velocity of 1 cm yr^{-1} . We define the linear moment \mathcal{M}_{lin} of a seismic event by:

$$\mathcal{M}_{\text{lin}} = G \int_{\text{fault}} s(x) dx, \quad (11)$$

which has the dimension of a moment per unit of length. The corresponding linear magnitude M_{lin} of each of the seismic events on the fault is defined as:

$$M_{\text{lin}} = \frac{2}{3} \log_{10} \mathcal{M}_{\text{lin}} - 6.07, \quad (12)$$

and is indicated in Fig. 4(a). In (11), $x \in [-1500; 1500]$ m is the position along the fault and $s(x)$ is the slip on the fault at position x . Note that initial conditions assumed on the fault affect only several first events; afterwards, the fault behaviour becomes independent of the initial conditions (e.g. Lapusta & Liu 2009). In Fig. 4(a) and

other similar figures, the first events shown occur after at least 100 other events that have been removed.

When evolving only under constant background loading, the fault can produce a fairly broad complexity of event sizes and earthquake patterns (Fig. 4). Some events rupture the entire seismogenic patch at once, still producing events of various magnitudes, while some smaller events only rupture an edge of the patch. The complexity produced by this fault is due to the fact that the critical size necessary to nucleate seismic events on the seismogenic patch is much smaller than the total length of the seismogenic patch. The critical nucleation size has been analysed in numerous studies (e.g. Ruina 1983; Dieterich 1992; Rubín & Ampuero 2005), and can be written as:

$$h^* = \frac{GD_c}{F(a, b)\sigma}, \quad (13)$$

where the function $F(a, b)$ of the fault parameters a and b refers to different models estimating the critical nucleation size, and is given by $F(a, b) = \pi(a - b)/2$ (Rice & Ruina 1983), $F(a, b) = b$ (Dieterich 1992), or $F(a, b) = b$ when $a/b < 0.37$ and $F(a, b) = \pi(b - a)^2/(2b)$ when $a/b > 0.5$ (Rubín & Ampuero 2005). In our case, $a/b \approx 0.67$, and taking the estimation by Rubín & Ampuero (2005) yields:

$$h^* = \frac{2}{\pi} \frac{b}{(b - a)^2} \frac{GD_c}{\sigma} \approx 15 \text{ m}. \quad (14)$$

In order to illustrate the event complexity, Fig. 4(b) represents the distribution of linear magnitudes of all the seismic events produced by this fault. To the first order, this distribution is bimodal: events with $M_{\text{lin}} > 0.75$ rupture the entire seismogenic patch while events with $M_{\text{lin}} < 0.75$ only rupture an edge of the seismogenic patch. As illustrated in Fig. 4(a), the fault exhibits irregularity, the fact supported in Fig. 4(b) by the existence of various peaks in the magnitudes distribution at $M_{\text{lin}} > 0.75$. Larger events of $M_{\text{lin}} \sim 1.05$ and $M_{\text{lin}} \sim 1.2$ alternate with smaller foreshocks and aftershocks with $M_{\text{lin}} < 0.75$ and sometimes other small events during the interseismic period (first 12 events in Fig. 4a), whereas events of $M_{\text{lin}} \sim 0.94$ that also rupture the entire patch seem to almost periodically follow each other without any smaller events in-between (events 13–18 in Fig. 4a).

This is even more obvious when looking at periodicities in the timing of events produced by this fault. Fig. 5 shows the Schuster spectrum (Ader & Avouac 2013) computed for the timing of the $\sim 15\,000$ events from the catalogue generated by the simulation. This spectrum shows the periodicities in the timings of events on the fault: peaks above the ‘99 per cent confidence level’ line indicate that a periodicity at the tested period exists in the timing of events in the catalogue at more than a 99 per cent level of confidence. The Schuster spectrum thus indicates that this fault has a natural periodicity around period of $T = 0.02$ yr. The periodicities at smaller periods are simply harmonics of this period (Ader & Avouac 2013).

To understand the origin of this natural periodicity, one can estimate the return period of events of a given linear moment \mathcal{M}_{lin} , by supposing that such events release all the moment deficit accumulated on the seismogenic patch from the constant loading:

$$T_{\text{RET}}(\mathcal{M}_{\text{lin}}) = \frac{\mathcal{M}_{\text{lin}}}{GWV_{\text{pl}}}, \quad (15)$$

where $W = 500$ m is the length of the seismogenic patch and $V_{\text{pl}} = 1 \text{ cm yr}^{-1}$ is the loading plate velocity. In terms of linear moment magnitude M_{lin} , and with the parameters of the simulation, eq. (15) becomes:

$$T_{\text{RET}}(M_{\text{lin}}) = 10^{1.5M_{\text{lin}} - 2.08} \text{ yr}. \quad (16)$$

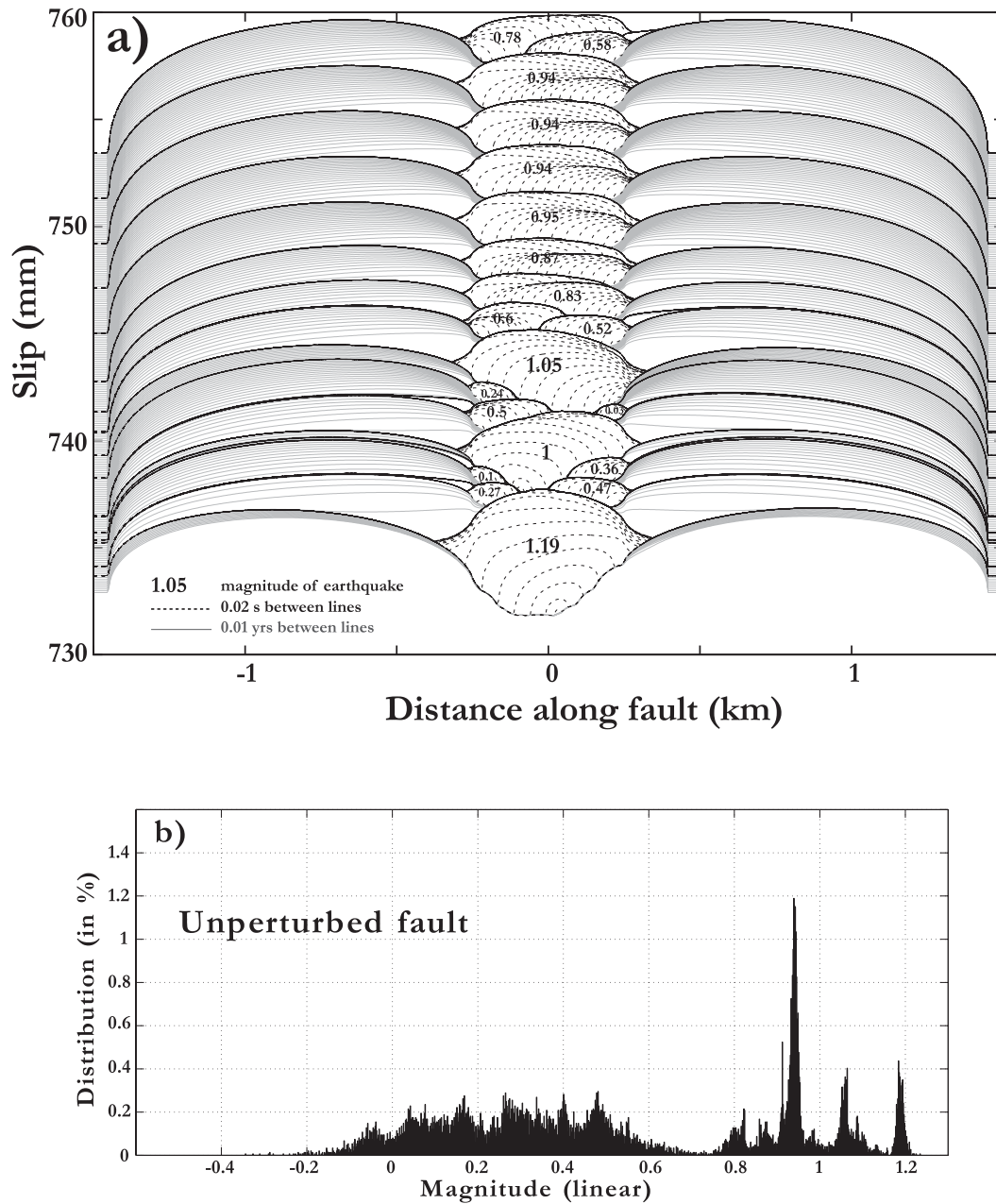


Figure 4. (a) Evolution of slip on the unperturbed fault with time. The linear magnitude of the seismic events produced is indicated on each event. If the fault is experiencing a seismic event, the slip on the fault is plotted every 0.02 s (dashed black lines), while during the interseismic period, slip is only plotted every 0.01 yr (plain grey lines). Black lines appear as coalescence of several dashed lines at the end of a seismic event. (b) Magnitude distribution of events produced by the fault. The earthquake catalogue contains a total of about 15 000 events, covering about 1700 yr of evolution of the fault.

Using eq. (16), the expected return periods of events rupturing the entire seismogenic patch corresponding to the main peaks in Fig. 4(b) would be $T_{\text{RET}}(M_{\text{lin}} = 0.94) \approx 0.21$ yr, $T_{\text{RET}}(M_{\text{lin}} = 1.05) \approx 0.31$ yr and $T_{\text{RET}}(M_{\text{lin}} = 1.2) \approx 0.53$ yr. Periods corresponding to the return periods of $M_{\text{lin}} = 1.05$ and $M_{\text{lin}} = 1.2$ events do not appear in the Schuster spectrum of the seismicity, indicating that events of magnitude $M_{\text{lin}} > 1$ happen in a fairly chaotic manner. The strong periodicity appearing at 0.2 yr in Fig. 5 corresponds to the expected return period of $M_{\text{lin}} \sim 0.94$ events, implying that these happen at quite regular time intervals on the fault.

5 RESPONSE OF A RATE-AND-STATE SEISMOGENIC FAULT TO HARMONIC SHEAR-STRESS PERTURBATIONS

5.1 Method

In order to study the response of the fault presented in the previous section to harmonic stress perturbations, we simulate the evolution of the slip on this fault with the exact same fault parameters as previously described, while superimposing a harmonically varying

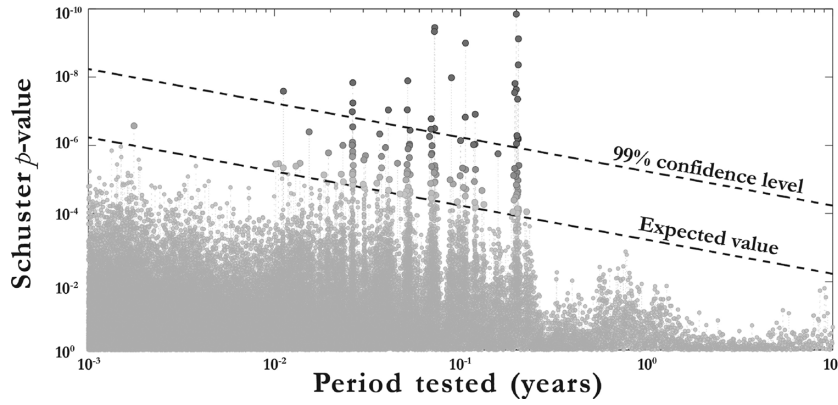


Figure 5. Schuster spectrum for the unperturbed fault (Fig. 4). The spectrum is computed for the timing of about 15 000 events spanning 1700 yr of history on the fault. The Schuster p -value indicates the probability that a periodicity is observed by chance in the timing of events. The ‘expected value’ line indicates the expected value of the Schuster p -value, while points above the ‘99 per cent confidence level’ line have a probability above 99 per cent to be real periodicities in the catalogue, rather than being observed by chance. The periodicity at $T \approx 0.2$ yr corresponds to the return period of events with $M_{\text{lin}} \approx 0.94$, indicating that these events happen quite periodically on the fault, while periodicities at smaller periods are harmonics of this period.

stress over the entire fault (both the rate-strengthening and the rate-weakening parts):

$$\Delta\tau(t) = \Delta\tau \sin \omega t, \quad (17)$$

where the amplitude of the stress perturbation is held constant at $\Delta\tau = 3$ kPa, as inferred for Nepal (Bettinelli *et al.* 2008). The ratio $\Delta\tau/a\sigma = 0.075 \ll 1$ indicates that we are in the case of small perturbations, according to Section 3. We run simulations for perturbations at periods varying between 10^{-6} and 10 yr. In order to estimate the amplitude of the variations of seismicity and their phase, we stack the times of N events from the simulated catalogue over the perturbing period. We then compute the seismicity rate over the perturbing period T by dividing the period into $B = 32$ bins of equal duration T/B and counting the number of events falling within each bin. We finally normalize this stacked seismicity rate by its mean, so that the average seismicity rate is equal to 1. Given the number of events N in the catalogue and the number of bins B , the variance of the normalized number of events falling within each bin is (e.g. Ader & Avouac 2013):

$$\sigma_B^2 = (B - 1)/N. \quad (18)$$

For each simulated catalogue, we then fit the seismicity rate with a function qualitatively following the predictions of Dieterich (1994):

$$\frac{R(t)}{r} = \frac{e^{\beta \sin(\omega t - \Phi)}}{\langle e^{\beta \sin \omega t} \rangle}, \quad (19)$$

where the amplitude β and phase Φ of the response are determined to fit the results of each simulation. Note that β is equal to $\Delta\tau/a\sigma$ according to the SRM for periods smaller than T_a ; here, we do not impose β but rather determine it from the simulation results. The notation $\langle \cdot \rangle$ refers to the mean of the function.

Fig. 6 illustrates this process: it shows, for four different simulations with different perturbing periods, the stacked seismicity rate (black circles with error bars corresponding to σ_B in eq. 18) and the result of the fit. This figure shows that, although the perturbation is of a small amplitude, the resulting variations of the seismicity rate can actually be fairly large, and that a phase shift appears as the perturbing period increases (recall that the shear-stress perturbation is a sine function, and so it is 0 at time equals 0). The amplitude of the seismicity-rate variations thus appears to be dependent on the perturbation period in a non-monotonic manner, being higher at $T = 0.027$ yr than at both $T = 0.0027$ and 1 yr.

In order to estimate uncertainties on β and Φ , we use analytical estimates for the case of small variations of the seismicity rate, that is, $\beta \ll 1$. In this case, eq. (19) can be linearized:

$$\frac{R(t)}{r} = 1 + \beta \sin(\omega t - \Phi) = 1 + m_1 \sin \omega t + m_2 \cos \omega t, \quad (20)$$

where m_1 and m_2 are two linear parameters determined by the fit to the seismicity rate, such that $\beta = \sqrt{m_1^2 + m_2^2}$ and $\Phi = \arctan(m_2/m_1)$. With parameters m_1 and m_2 , the fit is linear and the covariance matrix associated to the vector of parameters $[m_1, m_2]$ is:

$$C_M = 2 \frac{B - 1}{BN} \mathcal{I}_2, \quad (21)$$

where \mathcal{I}_2 is the 2×2 identity matrix. Given that the expected variance of the residuals is N/B (e.g. Ader & Avouac 2013), in order to account for the misfit of eq. (20) to the seismicity rate, the covariance matrix C_M is multiplied by $\text{var}(\text{residuals}) \times B/N$ if the variance of the residuals $\text{var}(\text{residuals})$ is greater than N/B . The uncertainties on β and Φ are finally computed from the obtained covariance matrix. This method may underestimate the errors on β when the linear condition $\beta \ll 1$ is not verified, but in practice it yields a good orders-of-magnitude estimate for the uncertainties. In Fig. 6, for instance, the case $T = 0.1$ yr is the most pathological and yields $\beta \approx 1.7 \pm 0.12$. The uncertainty on β is thus probably underestimated, but it is unimportant for our conclusions, since all β indicates is that the level of the response of seismicity is high.

5.2 Dependence on the period of the shear-stress perturbation

The procedure of Section 5.1 is repeated for different perturbing periods (Fig. 7). We plot both the amplitude of the seismicity-rate variations (parameter β in eq. 19) and their phase shift (parameter Φ in eq. 19) for the different values of the perturbation’s period. The amplitude plot has been normalized by the maximum possible amplitude according to the SRM, that is, $\beta_{\text{SRM}} = \Delta\tau/a\sigma$. The predictions of the SRM are indicated for comparison as a dashed grey line, where we have taken $2\pi t_a = 0.1$ yr in order to approximately fit the phase change from the simulations in Fig. 7. This value of t_a is quite arbitrarily selected at this stage, because the secular stress

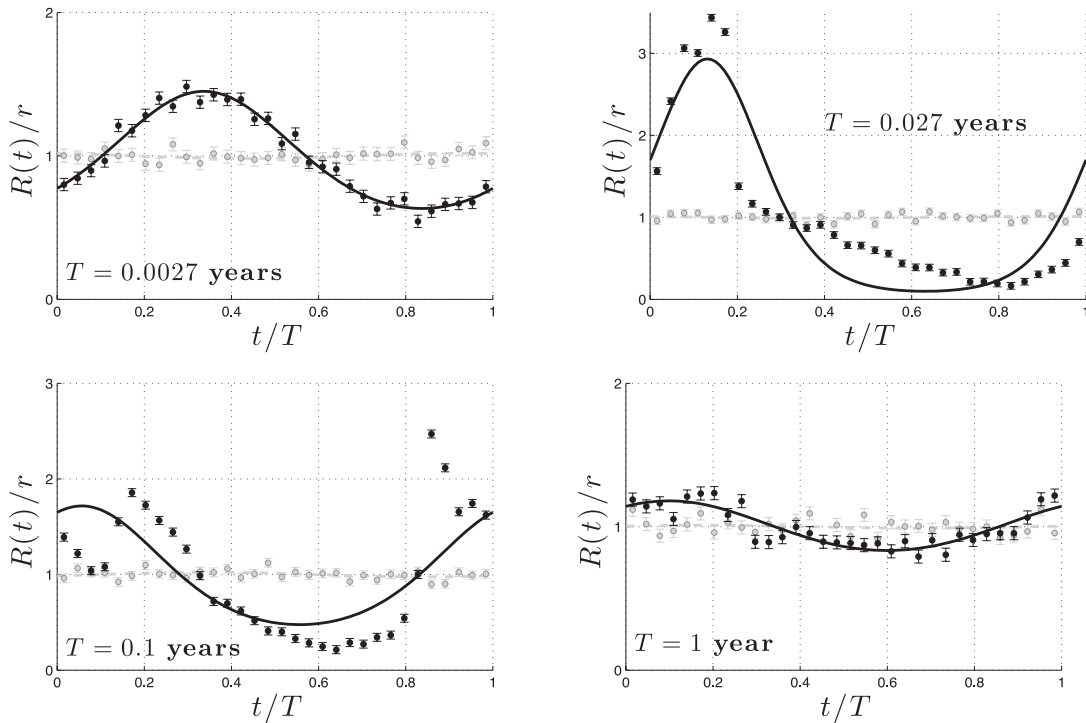


Figure 6. Stacked seismicity rate (black dots with error bars) and its fit with eq. (19) (black line). The grey circles with error bars and dashed grey line show the seismicity rate from the unperturbed catalogue stacked over the same period and the corresponding fit. The seismicity rate is normalized by its average, so that the quantity plotted is $R(t)/r$. The error bars on the seismicity rate only depend on the total number of events N in the catalogue and the number B of bins used to compute the stacked seismicity rate: $\sigma_B = \sqrt{(B-1)/N}$ (e.g. Ader & Avouac 2013). The period of perturbation T is indicated on each plot.

loading rate $\dot{\tau}_a$ and thus t_a are not as well defined for a finite fault as for the SRM, since in the case of a finite fault, $\dot{\tau}_a$ varies both in space and time. The harmonic response of the finite fault plotted in Fig. 7 displays features in agreement with the predictions of the SRM, but also major qualitative and quantitative differences.

There are two important differences between the response of the finite fault in our simulations and the SRM. First, the dependence of the finite-fault seismicity response on the perturbation period is non-monotonic, with a pronounced peak. We will denote the period at which the seismicity peaks by T_a . Note that the existence of such a peak may explain the differences between the response of the seismicity in the Himalaya to seasonal perturbations and tides, provided that the period T_a is close to 1 yr and hence the fault is more sensitive to the seasonal perturbations than perturbations of smaller periods. In Fig. 7, $T_a \approx 0.03$ yr, not yet appropriate for explaining the response in the Himalaya, and that is why we investigate the dependence of T_a on the model parameters in the following sections. Second, the amplitude of the seismicity response for the finite fault is always much larger than the predictions of the SRM. As discussed in Section 7.2, this finding means that the values of $a\sigma$ estimated from observations using the SRM model are probably systematically underestimated.

At the same time, as predicted by the SRM, one can identify two regimes of seismicity response, depending on whether the period T of the perturbation is larger or smaller than the critical period T_a , at which the amplitude of the seismicity response peaks. At periods $T < T_a$, variations of the seismicity rate tend to be in phase with the stress perturbation ($\Phi \sim 0$), although a gradual time lag from 0 to about $-\pi/4$ appears as the period increases, which is not expected in the SRM. On the other hand, for periods $T \geq T_a$, the seismicity

rate appears to correlate with the rate of shear-stress perturbation, since the phase is $\Phi \sim \pi/2$ and the amplitude decreases following a $1/T$ trend. At these periods, the response of the seismicity rate is thus analogous to the Coulomb failure type of response, as predicted by the SRM at periods $T \gg t_a$.

In order to better understand the high sensitivity of the finite fault to stress variations, we examine in more detail the seismicity produced by the perturbed fault. Fig. 8 shows the distribution of event magnitudes produced by the harmonically perturbed fault, at periods $T = 0.0027, 0.027$ and 1 yr. This figure should be compared to Fig. 4, which shows the distribution of event magnitudes on the unperturbed fault. At period $T = 1$ yr, the fault responds in a Coulomb-like fashion (Fig. 7) and the distribution of magnitudes on the fault is quite similar. However, for the perturbation periods shorter than T_a ($T = 0.0027$ and 0.027 yr), the distribution of magnitudes is considerably modified. The fault only produces either events of magnitude $M_{\text{lin}} \sim 1.05$ rupturing the entire seismogenic patch or events with $-0.4 \leq M_{\text{lin}} \leq 0.4$, that is smaller on average than the events usually produced by the unperturbed fault, which have magnitudes $-0.2 \leq M_{\text{lin}} \leq 0.6$. Events of magnitude $M_{\text{lin}} \sim 0.94$ that form a stable pattern on the unperturbed fault have completely disappeared from the seismicity on the fault perturbed at periods $T < T_a$.

Fig. 9 shows the Schuster spectra of the seismicity on the faults perturbed with the same three periods as in Fig. 8. Except for a prominent peak at 1 yr caused by the response of the seismicity to the stress perturbation, the spectrum of the fault perturbed with period $T = 1$ yr (lower plot in Fig. 9) is essentially the same as the spectrum of the unperturbed fault in Fig. 5. The periodicity at $T \approx 0.2$ yr, corresponding to the return period of $M_{\text{lin}} \sim 0.94$ events, is still in the spectrum, although not as prominent as in the

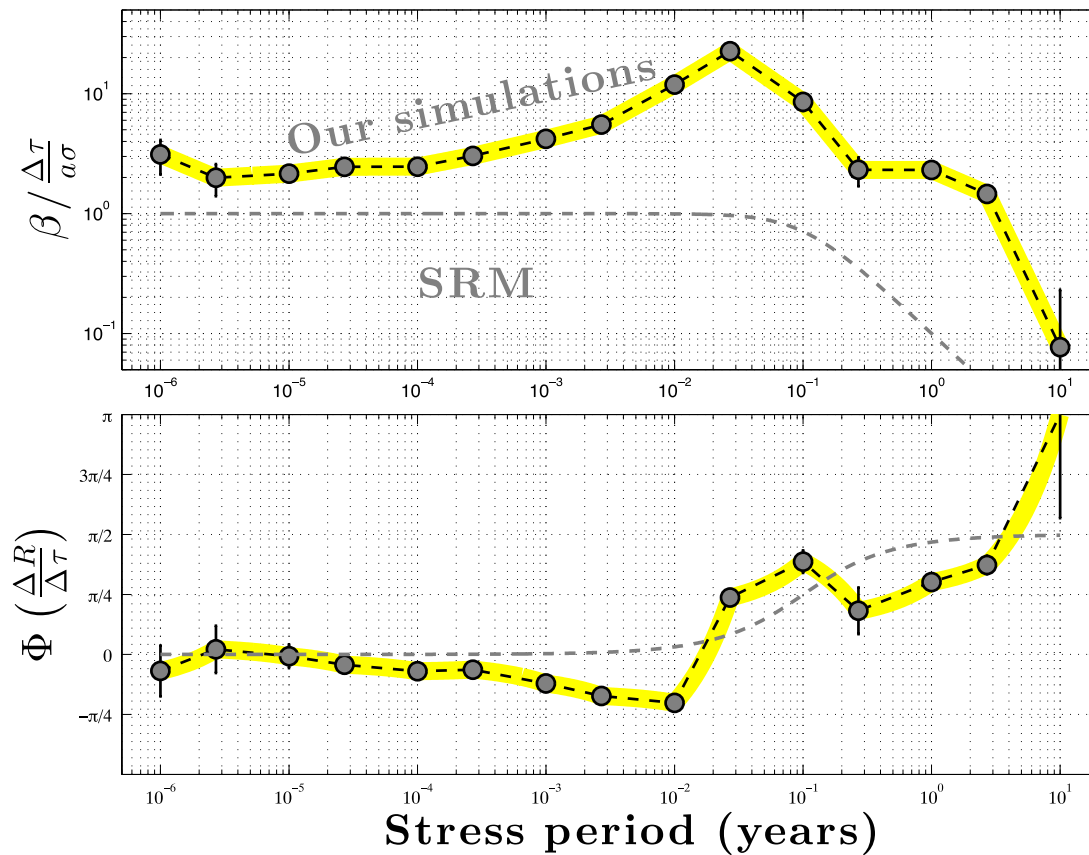


Figure 7. Response of a finite rate-and-state fault to harmonic shear-stress perturbations. Each point on the plot corresponds to a simulation which generated an earthquake catalogue. The times of events from the catalogue are stacked over one period and the resulting stacked seismicity rate is fitted with eq. (19). The value obtained for β is reported on the upper plot, while the phase shift Φ between the seismicity rate and the stress is represented on the lower plot. Dashed grey curves show the predictions of the SRM, where we have taken $2\pi t_a = 0.1$ yr in order to fit the phase. As in the SRM, one can separate two regimes of response, depending on whether the perturbing period is shorter or greater than a critical period T_a . However, the amplitude of the response is always greater than predictions from the SRM, sometimes by more than an order of magnitude, and this amplitude of the response increases with the period T for periods $T < T_a$.

unperturbed case. The timing of these events is most likely slightly affected by the perturbation and they do not happen as periodically as in the unperturbed case. The Schuster spectra for faults perturbed at periods $T = 0.0027$ and 0.027 yr are much different from the spectrum of the unperturbed case (Fig. 5). As expected, they have prominent periodicities at the perturbing periods and at some harmonics of the perturbing period (the y -axis has been saturated, the corresponding Schuster p -values are much smaller than what can be read on the spectra), but they also exhibit very low Schuster p -values at periods around 0.33 yr, which, as indicated earlier, approximately corresponds to the return period of $M_{\text{lin}} = 1.05$ events on the fault. As highlighted earlier, these $M_{\text{lin}} \sim 1.05$ events now constitute all of the events produced on the fault that rupture the entire seismogenic patch. Although they used to happen in a fairly chaotic way on the unperturbed fault, the strong periodicity at their return period indicates that they now occur fairly regularly. The characteristics of the seismicity on the fault are thus drastically changed when the fault undergoes harmonic stress perturbations at periods $T < T_a$, consisting exclusively of large $M_{\text{lin}} = 1.05$ events, almost systematically followed by two small aftershocks, with the rare occurrence of small events during the interseismic period (this is obvious when looking at the slip on the fault in this case, supplementary Fig. S1). The perturbation seems to have stabilized the seismic cycles dominated by $M_{\text{lin}} = 1.05$ events, while the seismic

regime that was stable in the case of an unperturbed fault (repeating $M_{\text{lin}} \sim 0.95$ events) has literally disappeared from the seismicity. The fault also now seems unable to produce larger $M_{\text{lin}} \sim 1.2$ events.

This highlights a first major conceptual difference between the finite-fault simulations and the SRM, with the latter assuming that the stress perturbation simply modifies the timing of events on the fault. Our simulations suggest that, beyond a mere change in the timing of events, the entire set of characteristics of the earthquake population produced by the fault is modified. This might explain why the response of the seismicity is much larger in the case of the finite fault than with the SRM. The modification of the seismicity pattern by the perturbation is even more obvious when studying a fault with a smaller seismogenic patch. Fig. 10 shows the slip on a fault of the same size (3 km), but where the seismogenic patch is 200 m long. The unperturbed fault (Fig. 10a) only produces one type of an earthquake, repeating with the exact same magnitude and at constant time intervals. This repeat period is directly related to the size of the seismogenic patch (Fig. S7). The seismicity produced is much less diverse than the one produced by a fault with a 500 m long patch. This is because the ratio of the fault size to the nucleation size is smaller for the shorter patch. However, when a small harmonic perturbation is applied, the seismicity produced by the 200 -m-long patch becomes diversified (Fig. 10b). The patch starts to produce events that rupture the entire seismogenic patch

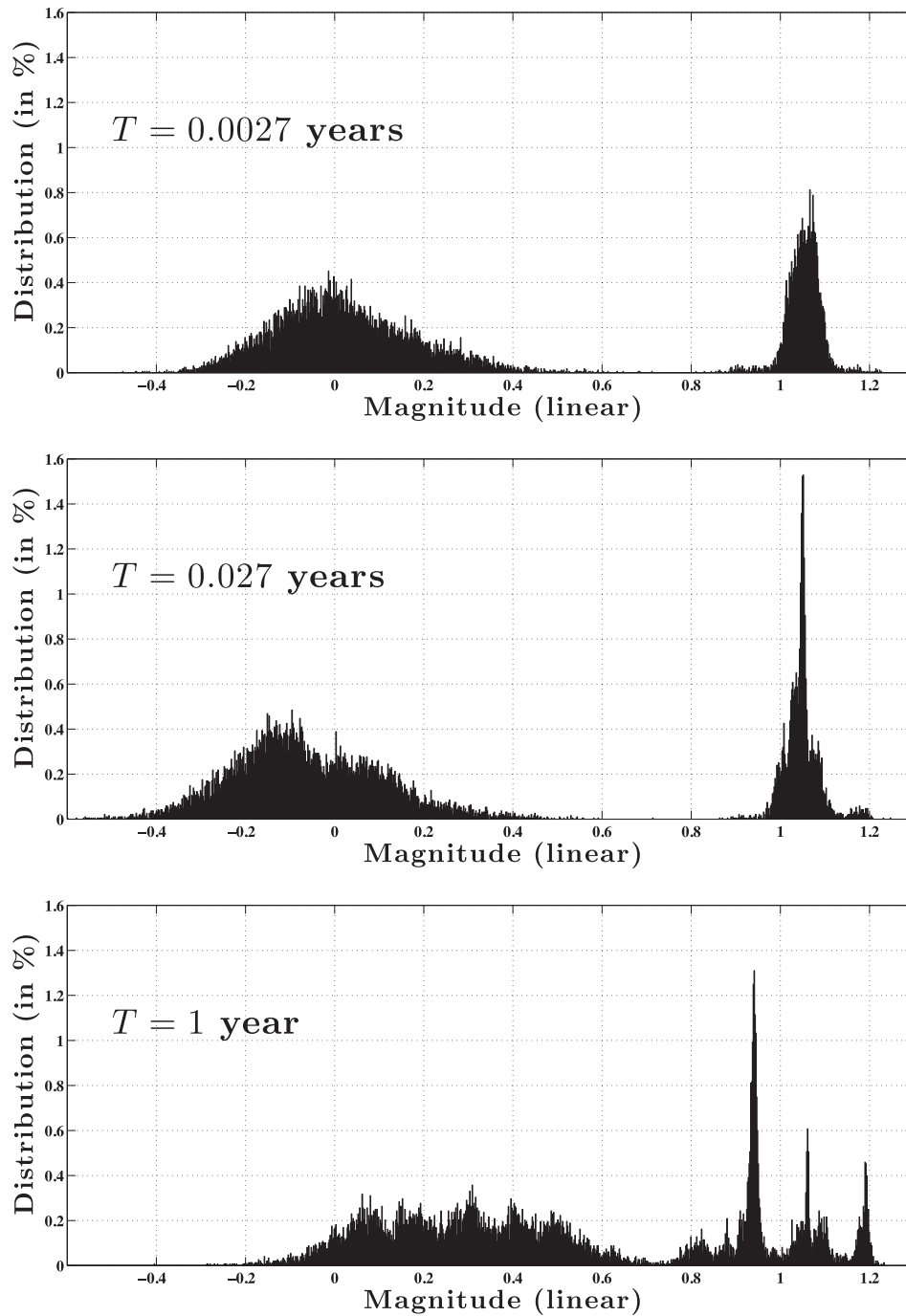


Figure 8. Magnitude distribution of events happening on a fault loaded at $V_{pl} = 1 \text{ cm yr}^{-1}$ (i.e. grey circles in Fig. 7), for harmonic shear-stress perturbations at periods $T = 0.0027 \text{ yr}$, $T = 0.027 \text{ yr}$ (thus $T < T_a$) and $T = 1 \text{ yr}$ ($T > T_a$). The other simulation parameters are the same as for Fig. 4. While the distribution of magnitudes produced by the fault perturbed at 1 yr is essentially the same as the one of the unperturbed fault (Fig. 4), the distribution is very different for the two faults perturbed at periods $T < T_a$. The fault perturbed at $T < T_a$ produces smaller events than the unperturbed fault, and events that rupture the entire seismogenic patch all have $M_{lin} \sim 1.05$. In particular, $M_{lin} \approx 0.94$ and $M_{lin} \sim 1.2$ events have almost completely disappeared from the seismic population produced by the fault.

and events that only happen at the edges, so that the seismicity distribution covers a larger range of magnitudes. Even more clearly here than with the 500 m patch, the introduction of an external harmonic perturbation does much more than simply affecting the timing of events: it modifies the type of earthquakes that the fault can produce.

5.3 On the critical perturbation period on a finite fault

As Section 5.2 shows, both our finite-fault model and the SRM exhibit two regimes in their response to harmonic stress perturbations: the seismicity correlates with the stress perturbation at periods T shorter than T_a , whereas it correlates with the stress-rate perturbation at periods T larger than T_a . In the SRM, the characteristic period

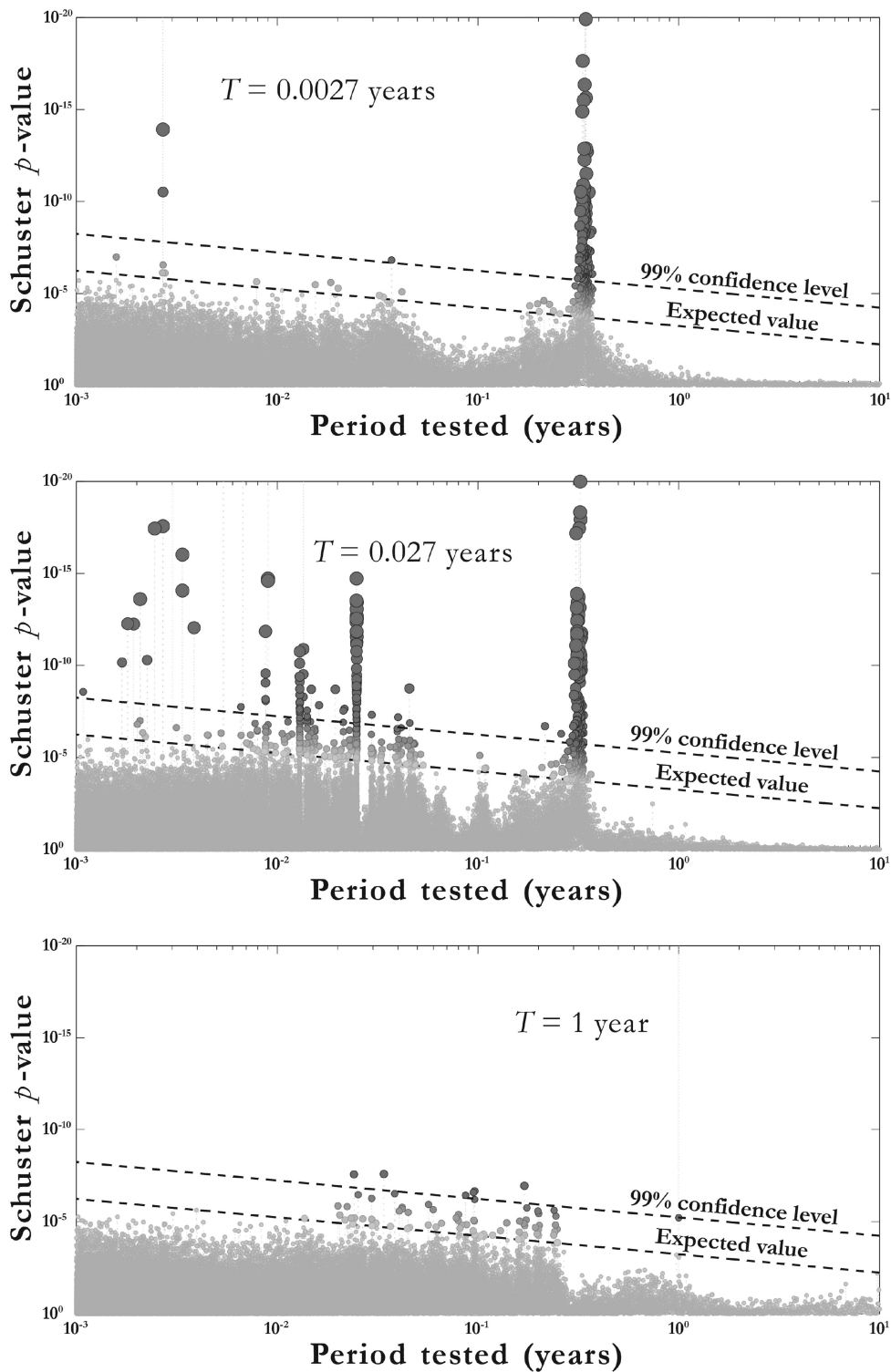


Figure 9. Schuster spectra for timing of events happening on a fault loaded at $V_{pl} = 1 \text{ cm yr}^{-1}$ (i.e. grey circles in Fig. 7), for harmonic shear-stress perturbations at periods $T = 0.0027 \text{ yr}$, $T = 0.027 \text{ yr}$ and $T = 1 \text{ yr}$. Other simulation parameters are the same as for Fig. 7. We saturated the y -axis at 10^{-20} in order for the plots to be readable. For the perturbations at $T = 0.0027 \text{ yr}$ (upper plot), the Schuster p -value at the perturbing period goes up above 10^{-150} . For the perturbations at $T = 0.027 \text{ yr}$ (middle plot), the Schuster p -value at the perturbing period goes up to about 10^{-2150} , and all the first harmonics go up to values above 10^{-100} . For the perturbation at $T = 1 \text{ yr}$ (lower plot), the Schuster p -value at the annual period goes up to about 10^{-50} . Except for the prominent peak at $T = 1 \text{ yr}$, the spectrum of the fault perturbed at 1 yr (lower plot) is very similar to the spectrum of the unperturbed fault in Fig. 5. The spectra of faults perturbed at $T < T_a$ (upper and middle plot), exhibit a prominent peak at $T = 0.33 \text{ yr}$, which is approximately the return period of $M_{lin} = 1.05$ events, indicating that these now happen in a quasi-periodic way on the fault.

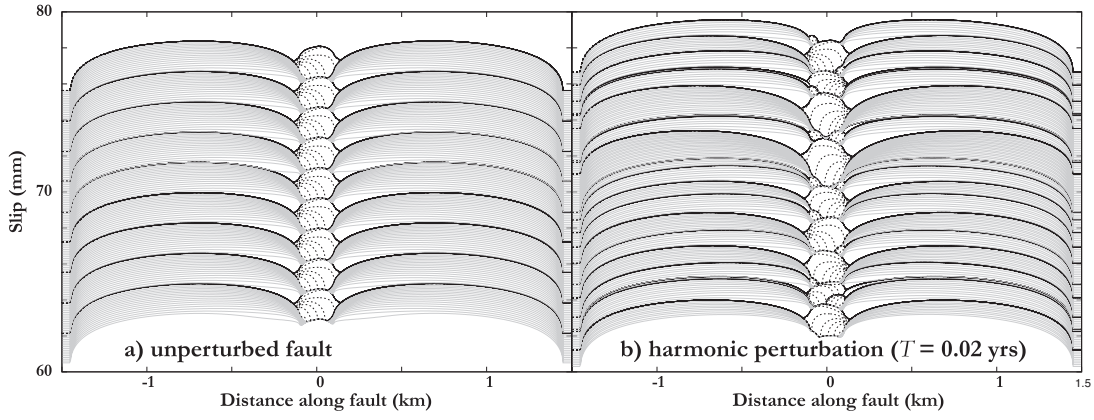


Figure 10. Unperturbed and perturbed slip evolution of a fault. (a) Unperturbed evolution of the fault, which has the same properties as the fault in Figs 4 and 7, except that the seismogenic patch is only 200 m long. In this case, the fault only produces one type of an earthquake, at equally spaced time intervals (return period of about 0.17 yr). (b) Slip on the fault when it is perturbed with a harmonically varying shear stress with period $T = 0.02$ yr and amplitude $\Delta\tau = 3$ kPa. The seismicity produced by the perturbed fault is much different, illustrating that the perturbation may have a much broader impact on the seismicity produced by the fault than just inducing a simple modification of the timing of events.

separating the two regimes is $T_a = 2\pi t_a = 2\pi a\sigma/\dot{\tau}_a$, as eq. (8) indicates, where the secular shear-stress rate is $\dot{\tau}_a = kV_{pl}$, k being the spring stiffness.

Hence a natural approach to investigating T_a for a finite fault would be to examine how the dependence of T_a on model parameters differs from that predicted by the SRM. The main issue in adapting eq. (8) for the finite fault is the fact that whereas k and $\dot{\tau}_a$ are constant in space and time and thus well defined in the SRM, they are not in the finite-fault model. Depending on where and when on the seismogenic patch one measures the shear-stress rate, the value varies a lot (Fig. S2). Similarly, the relevant slip-zone size that determines k may vary in the finite-fault model. Note that decreasing the size of the creeping zone by a factor of 2 does not modify the response of the seismogenic patch to a harmonic perturbation (see Fig. S4 for a comparison when the size of the creeping zone is divided by 2), indicating that, as long as the rate-strengthening zone is large enough to prevent any boundary effects, its actual size does not influence the behaviour of the seismogenic patch, and hence does not influence the relevant shear-stress rates.

To estimate $\dot{\tau}_a$ in our model, let us consider a simplified anti-plane model in which a seismogenic patch of size W is locked and the areas outside are moving steadily with V_{pl} . In this case, the shear-stress rate within the patch can be computed from the shear-stress transfer (e.g. Freund 1990) and it is given by:

$$\dot{\tau}_a = \frac{G}{2\pi} \frac{V_{pl}W}{(W/2)^2 - z^2}, \quad (22)$$

where G is the shear modulus and $z = 0$ corresponds to the middle of the seismogenic patch. Since the effect of the perturbations is most likely to alter the nucleation process, and the nucleation occurs close to the edges of the seismogenic patch, we are interested in the values of z close to $W/2$; denoting $H = W/2 - |z|$ and simplifying expression (22) for $H < W/2$, we get:

$$\dot{\tau}_a = \frac{G}{2\pi} \frac{V_{pl}}{H}, \quad (23)$$

where H is the distance of interest from the creeping edges of the fault. Note that this expression has the intuitive structure of $\dot{\tau}_a = k_{ff}V_{pl}$, where $k_{ff} = G/(\pi H)$ is the equivalent finite-fault stiffness. Since we are interested in the locations within the nucleation region, we take $H = \kappa h^*$, where h^* is the critical nucleation size defined in eq. (13) and κ is a factor of the order of one. Using the estimate

for h^* from Rubin & Ampuero (2005) leads to the shear-stress rate of $\dot{\tau}_a = 4.2/\kappa$ MPa yr⁻¹, consistent with the values from our simulations (Fig. S2).

The critical period $T_a = 2\pi t_a = 2\pi a\sigma/\dot{\tau}_a$ is then given by:

$$T_a = 4\pi^2 \kappa \frac{a}{F(a, b)} \frac{D_c}{V_{pl}}, \quad (24)$$

where h^* has been replaced by its estimate (13).

Eq. (24) yields several predictions for the dependence of T_a on the different physical parameters of the problem. It predicts that T_a should be (1) inversely proportional to V_{pl} , (2) proportional to D_c , (3) independent on the effective normal stress σ .

Another possibility for explaining T_a is based on the study of Perfettini *et al.* (2001). Considering the behaviour of a spring-and-slider system with rate-weakening rheology, Perfettini *et al.* (2001) demonstrated the possibility of a resonance of the slip rate in the nucleation zone with a harmonic perturbation of normal or shear stress at the critical period

$$T_c = 2\pi \sqrt{\frac{a}{b-a}} \frac{D_c}{V_N}, \quad (25)$$

where V_N is the loading velocity on the slider. Note that the difference between the study of Perfettini *et al.* (2001) and the SRM model of Dieterich (1994) is the different assumptions about the state of the slider being perturbed; it is in steady-state sliding, $V\theta/D_c = 1$, for Perfettini *et al.* (2001) and in the state of acceleration with the assumption $V\theta/D_c > 1$ in the SRM. The assumption of Perfettini *et al.* (2001) is close to what occurs in finite-fault nucleation zones, where points away from the tips of the zone are in nearly steady sliding (Rubin & Ampuero 2005) (Fig. S3). Note that the dependence of T_c on D_c and loading velocity, and the absence of the dependence on σ , are the same as those in eq. (24).

In the following sections, we therefore investigate the dependence of T_a on the different parameters of the problem predicted by eq. (24).

5.4 Influence of the background loading rate V_{pl}

In order to see how the secular loading rate V_{pl} affects the frequency response of the finite fault, we look at the frequency response under different loading velocities. In the case of the finite fault, the relation

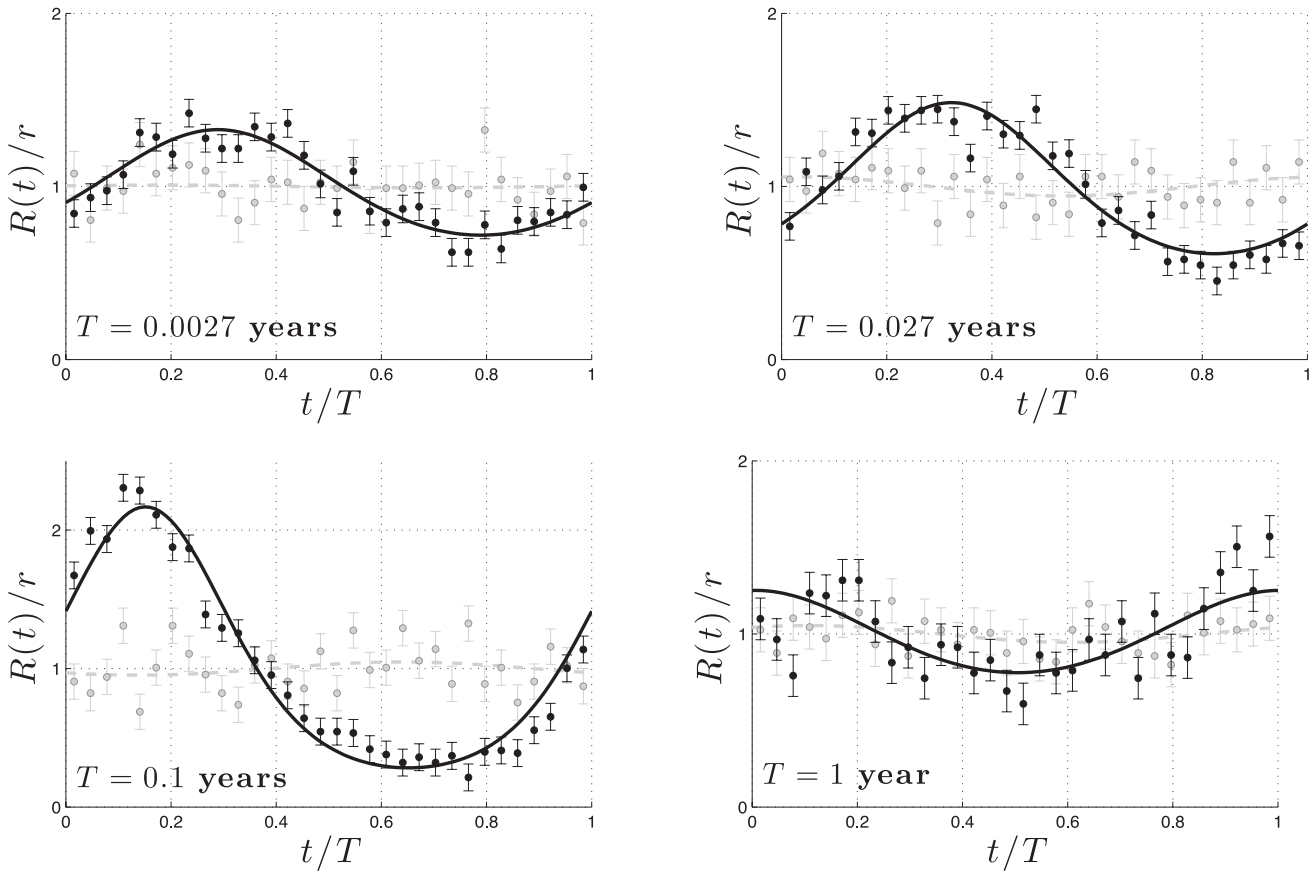


Figure 11. Stacked seismicity rate (black dots with error bars) and its fit with eq. (19) (black line) for $M_{\text{lin}} > 1$ events only. This plot is similar to Fig. 6, except that we only select $M_{\text{lin}} \geq 1$ events. Eq. (19) fits the seismicity rate quite well, indicating that the SRM describes qualitatively well the seismicity rate on the perturbed fault for events rupturing the entire seismogenic patch.

$\dot{\tau}_a = kV_{\text{pl}}$ is not well defined, since $\dot{\tau}_a$ varies in space and time. For example, when an event ruptures the entire patch, the following events often happen concurrently with the afterslip of this initial event, and therefore under a higher local $\dot{\tau}_a$. As a result, in order to single out the effect of the secular loading, we look at the response of $M_{\text{lin}} > 1$ events, which are spaced out in time and for which afterslip does not have any effect. These events thus happen only under the loading due to the constant loading velocity applied at the edges of the fault.

The stacked seismicity rate for these large events is represented in Fig. 11 for the same periods as in Fig. 6. In this case, eq. (19) gives a good fit to the seismicity rate at all periods, indicating that the SRM provides a good qualitative representation of the seismicity.

Looking at the quantitative response, Fig. 12 shows the response of $M_{\text{lin}} > 1$ events to harmonic perturbations of shear stress, for different values of the background loading velocity: the pink squares with the red line show the response for $V_{\text{pl}} = 10 \text{ cm yr}^{-1}$, the grey circles with yellow line show the response for $V_{\text{pl}} = 1 \text{ cm yr}^{-1}$ and the blue triangles with the blue line show the response for $V_{\text{pl}} = 0.1 \text{ cm yr}^{-1}$. For all these values of V_{pl} , the amplitude of the harmonic response at these magnitudes always remains much greater than the predictions of the SRM (dashed lines). Hence, even though eq. (19) provides a good qualitative representation of the variations of the seismicity rate for large events, the amplitude β of the response has to be much larger than the predictions of the SRM

in order to fit the seismicity rate variations, sometimes by several orders of magnitude.

In terms of the impact of the secular loading on the response of the fault to harmonic stress perturbations, V_{pl} influences both the amplitude of the response and the critical period T_a for which this amplitude is the largest (Fig. 12). The critical period T_a appears to be inversely proportional to the plate velocity V_{pl} , analogously to the inverse proportionality of t_a and $\dot{\tau}_a$ predicted by the SRM. The amplitude of the response, however, is not a simple translation along the periods axis as predicted by the SRM. The amplitude at the critical period T_a seems to increase as V_{pl} gets smaller. The difference is not obvious between loading velocities $V_{\text{pl}} = 1$ and 10 cm yr^{-1} , but the peak amplitude at $V_{\text{pl}} = 0.1 \text{ cm yr}^{-1}$ is about 2 orders of magnitude larger than at $V_{\text{pl}} = 1 \text{ cm yr}^{-1}$. Such a peak looks like a resonance at the characteristic return period of events T_{RET} , but would have no obvious reason to happen at $T = 1 \text{ yr}$ for $V_{\text{pl}} = 0.1 \text{ cm yr}^{-1}$, and not at $T = 0.1 \text{ yr}$ for $V_{\text{pl}} = 1 \text{ cm yr}^{-1}$, since $T_{\text{RET}} \propto 1/V_{\text{pl}}$ (eq. 15).

The inverse dependence of T_a on the loading rate appears in other features of the response of seismicity. For instance, comparing the frequency response of all and $M_{\text{lin}} > 1$ events for $V_{\text{pl}} = 1 \text{ cm yr}^{-1}$ (grey circles with yellow line in Figs. 7 and 12, respectively), the critical period T_a is higher for the response of $M_{\text{lin}} > 1$ events. This simply comes from the fact that smaller events (i.e. events that only rupture an edge of the seismogenic patch) often occur concurrently

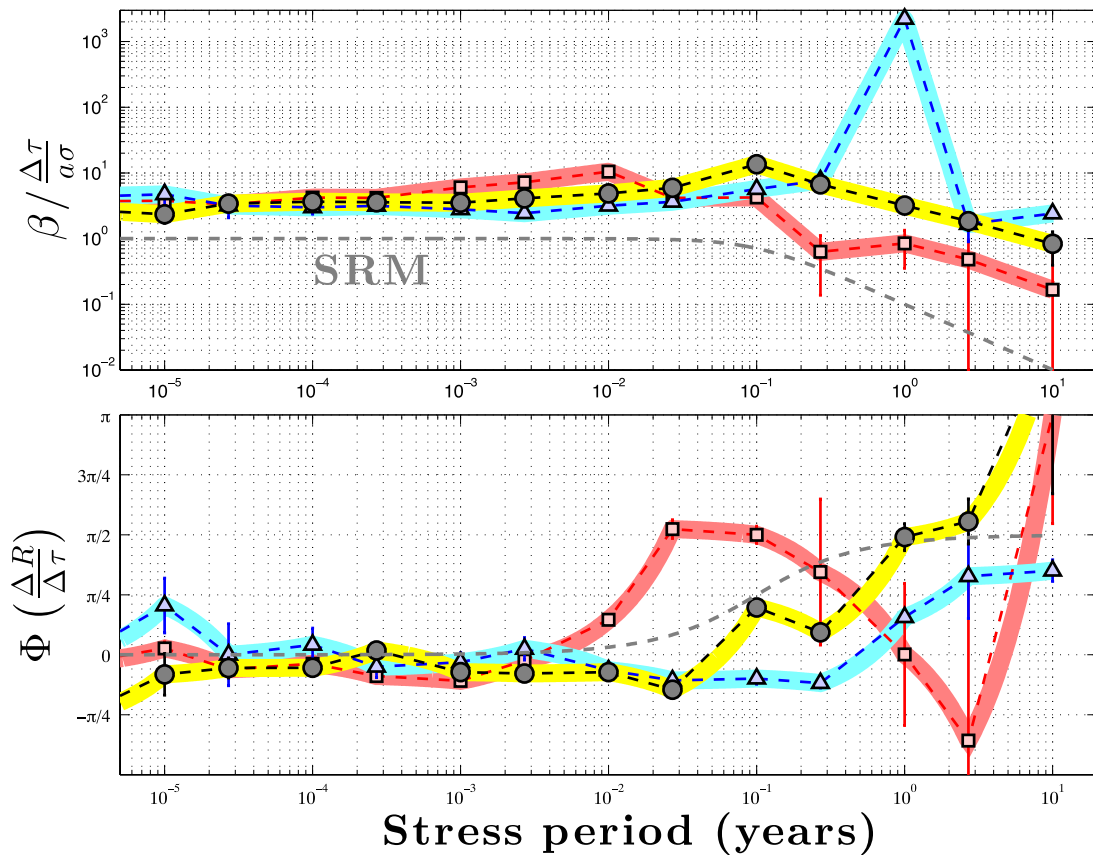


Figure 12. Response of a rate-and-state fault to harmonic shear-stress perturbations, for three different values of the plate loading velocity (blue triangles with the blue line: $V_{pl} = 0.1 \text{ cm yr}^{-1}$, black circles with yellow line: $V_{pl} = 1 \text{ cm yr}^{-1}$, pink squares with the red line: $V_{pl} = 10 \text{ cm yr}^{-1}$) for $M_{\min} \geq 1$ events. The other parameters of the simulation and the method to generate the plot are the same as in Fig. 7. The critical period T_a at which the amplitude of the response is the largest appears to be inversely proportional to V_{pl} , in qualitative accordance with predictions of the SRM. Interestingly, the value of V_{pl} has an impact on the amplitude of the frequency response, especially at the critical period T_a .

with the afterslip of large events, and hence they experience a higher loading rate than larger events, and, assuming an inverse variation of T_a with τ_a , their apparent T_a is smaller. When looking at all events together (Fig. 7), since smaller events are more numerous than larger events, the global variations of seismicity rate on the fault are dominated by those of the smaller events, and therefore the apparent T_a is the one of the smaller events. This is explored in more details in Appendix C, where it is also discussed how a phase shift may occur when examining the response of aftershocks to the harmonic perturbation, and τ_a and therefore T_a gradually vary during afterslip.

5.5 Influence of the characteristic slip D_c and normal stress σ

Studying the influence of D_c is challenging, because varying the value of D_c on the fault has several implications. When D_c increases, eq. (13) indicates that the nucleation size of events increases proportionally. When the nucleation size is not small enough compared to the length of the seismogenic patch (typically, when the nucleation size becomes larger than a tenth of the length of the seismogenic patch), only events of similar magnitude occur, that rupture the whole patch. Such a regular seismicity has a different response to harmonic perturbations, with resonances appearing between the return period of events produced and the period of the perturbation,

and comparing the response of such a fault to the response of a fault able to produce a wide range of magnitudes becomes difficult. On the other hand, when D_c decreases, the size of the cohesive zone defined in eq. (10) decreases proportionally, and the cell size for the simulation has to be reduced accordingly, which requires longer simulation times, which become intractable for much smaller D_c . Therefore, the parameter D_c can only be varied within a limited range of values.

At the same time, both the size of the cohesive zone and the nucleation size are proportional to D_c/σ . In theory, varying D_c and σ so that the ratio D_c/σ remains constant should therefore result in both a constant nucleation size and a constant size of the cohesive zone, that is a constant cell size required to simulate the evolution of slip on the fault. Since such simulations alone cannot assess whether changes in the fault response are due to variations of D_c or σ , we therefore run simulations where we vary only D_c , simulations where we vary only σ , and simulations where we vary both D_c and σ together keeping the ratio D_c/σ constant. The last type of simulations lets us vary D_c over a wider range of values than the first two types of simulations.

First, we look at the response of the fault to harmonic perturbations for a reduced range of values of D_c ($D_c = 1, 2, 5$ and $10 \mu\text{m}$) keeping the other parameters constant. To avoid the effects with post-seismic slip and hence variable loading rates discussed in Section 5.4, here we analyze only the behaviour of the larger events that span the entire seismogenic patch. When varying D_c ,

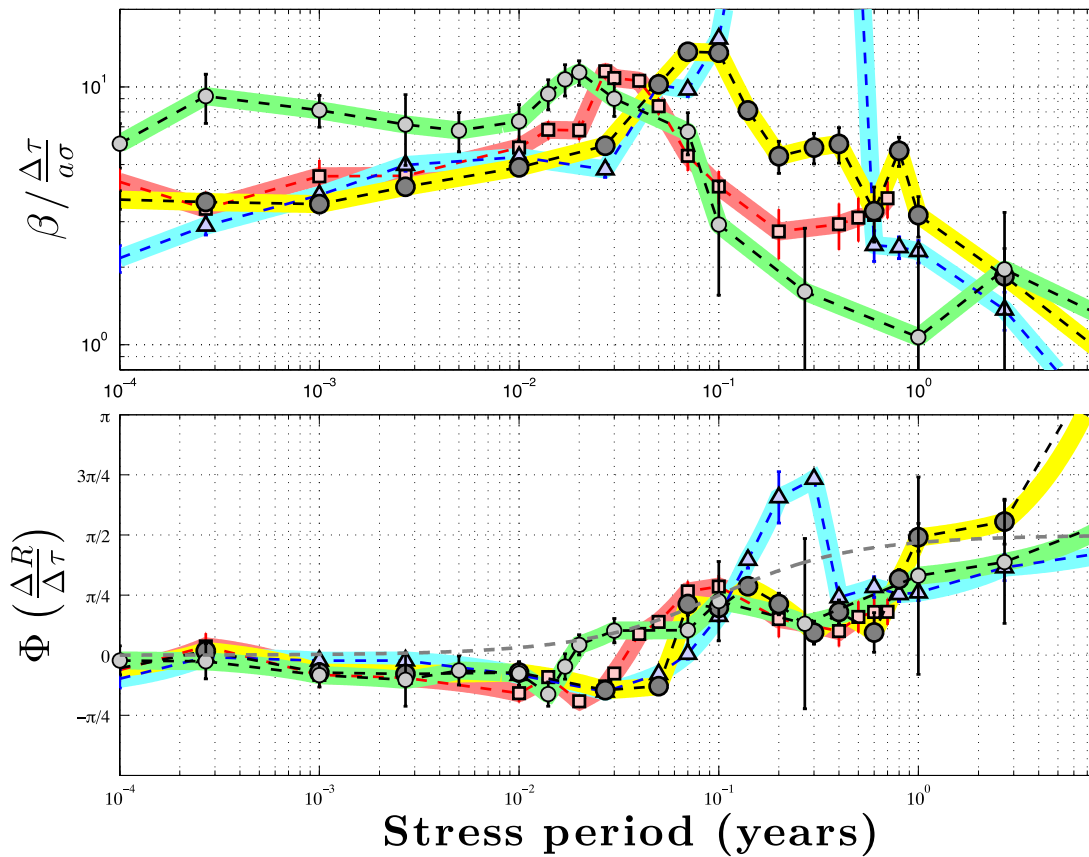


Figure 13. Response of a finite rate-and-state fault to harmonic shear-stress perturbations for four different values of the fault parameter D_c , for events rupturing the whole seismogenic patch. Other parameters are the same as in Fig. 7. Blue triangles with the blue line: $D_c = 10 \mu\text{m}$; black circles with yellow line: $D_c = 5 \mu\text{m}$; pink squares with the red line: $D_c = 2 \mu\text{m}$; light grey circles with green line: $D_c = 1 \mu\text{m}$. The critical period T_a at which the amplitude of the response is maximum is approximately proportional to D_c . The peak in amplitude in the case of $D_c = 10 \mu\text{m}$ is due to a resonance at the return period of typical events produced by the fault, which makes it dependent on the seismogenic segment size and hence different from T_a dependencies in other cases.

the characteristic period T_a at which the amplitude of the seismicity-rate variations is the largest seems to be approximately proportional to D_c (Fig. 13). Fig. 13 also indicates that the amplitude of the variations of the seismicity rate at perturbing period T_a increases with D_c , although this could be due to a period-sampling effect, that is the periods chosen for simulation.

The case of $D_c = 10 \mu\text{m}$ (blue triangles in Fig. 13) shows the complexity and non-linearity of the response, but actually does not provide much insight on the variation of T_a with fault properties. In this case, the nucleation size is too large for the unperturbed fault to produce a variety of magnitudes, and only $M_{\text{lin}} = 1.09$ events are produced at the regular return period of 0.38 yr. Some complexity happens when the fault is perturbed at periods smaller than this regular return period, similarly to the fault shown in Fig. 10. But when the fault is perturbed around the return period of events, the timing of seismic events starts to resonate with the perturbation and the amplitude of the response becomes quite large. The peak at 0.3 yr in Fig. 13 is due to this resonance, and is, in fact, an interesting feature. If there are sites on natural faults that result in such resonance, they would substantially contribute to the overall response of the area. However, such coincidences could be rare. Here, this resonance precludes us from determining T_a and the associated peak for this set of parameters if such a resonance did not exist (e.g. for a longer fault segment).

Note that in the cases of $D_c = 1, 2$ and $5 \mu\text{m}$, the period T_a is smaller than the characteristic return period of the patch-spanning

events produced on the fault. For $D_c = 5 \mu\text{m}$, the return period of events rupturing the whole patch (i.e. $M_{\text{lin}} \approx 1.05$ events) is about 0.31 yr and $T_a \approx 0.08$ yr, while for $D_c = 1$ and $2 \mu\text{m}$, the return period of the considered events is about 0.15 yr ($M_{\text{lin}} \approx 0.85$) whereas $T_a \approx 0.02$ or 0.03 yr. In these cases, the increase of the response amplitude is thus not due to a resonance with the natural return period of events. The fact that a resonance at the return period of the considered events may affect the determination of T_a is also illustrated in Fig. S8 in the supplementary material, where we compare the response of a fault with $D_c = 1 \mu\text{m}$ and $\sigma = 1$ MPa to stress perturbations of amplitude $\Delta\tau = 0.6$ kPa and $\Delta\tau = 3$ kPa. As can be seen from Fig. S8, the period of the resonance differs from T_a . Fig. S8 is also a good illustration of the non-linearity of the response of the finite fault with $\Delta\tau$.

Now that the influence of D_c alone has been examined, we vary D_c and σ together keeping the ratio D_c/σ and thus the nucleation size constant. In this case, we also vary the amplitude of the stress perturbation $\Delta\tau$ from one set of parameters to the other so that the ratio $\Delta\tau/a\sigma$ remains constant. Doing so over a wider range of values for D_c than previously explored ($D_c = 1, 5$ and $50 \mu\text{m}$), we again find that the characteristic period T_a is proportional to D_c , indicating that T_a varies with D_c but not with σ (Fig. 14). Besides, as before, the amplitude of the variations of seismicity rate at T_a seems to increase as D_c increases.

It is noteworthy that the phase associated with this response (lower plot in Fig. 14) seems to display anomalies, especially obvious

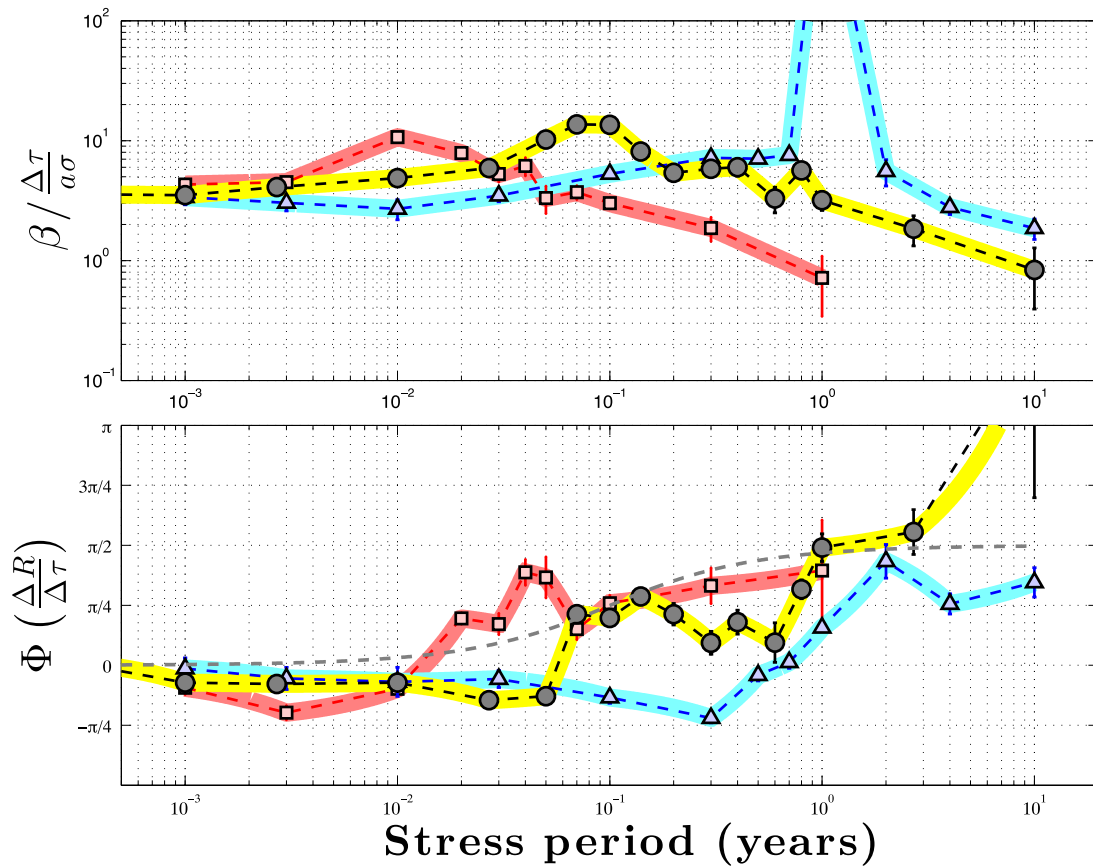


Figure 14. Response of a finite rate-and-state fault to harmonic shear-stress perturbations for three different values of the fault parameter D_c , as well as varying σ and $\Delta\tau$ to keep ratios D_c/σ and $\Delta\tau/a\sigma$ constant for the three simulations. Only events rupturing the whole seismogenic patch are used to compute the variations of seismicity rate. Blue triangles with the blue line: $D_c = 50 \mu\text{m}$; black circles with yellow line: $D_c = 5 \mu\text{m}$; pink squares with the red line: $D_c = 1 \mu\text{m}$. Other parameters of the simulation and the method to generate the plot are the same as in Fig. 7. Similarly to Fig. 13, the period T_a at which the amplitude of the response is maximum seems to be proportional to D_c .

around $T = 0.05 \text{ yr}$ for $D_c = 1 \mu\text{m}$ and around $T = 0.3 \text{ yr}$ for $D_c = 5 \mu\text{m}$. In the case $D_c = 1 \mu\text{m}$ and thus $\sigma = 1 \text{ MPa}$, the larger events produced by the fault have a magnitude of $M_{\text{lin}} \sim 0.5$ which would have a return period of $T(M_{\text{lin}} \sim 0.5) \approx 0.05 \text{ yr}$, according to eq. (16). Similarly, as has been mentioned earlier, the period $T = 0.3 \text{ yr}$ corresponds to the return period of large characteristic $M_{\text{lin}} \sim 1.05$ events produced by the fault when $D_c = 5 \mu\text{m}$ and thus $\sigma = 5 \text{ MPa}$. These anomalies in phase are thus most likely due to a resonance between the perturbing period and the natural return period of the considered events. This resonance can also be detected at a much lower level on the amplitude plot, without affecting the general trend of the response. This is why it is preferable to select the values of T_a from the amplitude response curve rather than the phase curve.

Finally, in order to validate the assessment that the critical period T_a does not depend on the normal stress σ , we simulate the response of the finite fault for different values of σ , holding all other parameters constant. As eqs (10) and (13) suggest, this exposes us to the same challenges as varying D_c in terms of the impact on the nucleation size and the size of the cohesive zone. Fig. 15 displays the response of the fault with $\sigma = 5, 12.5$ and 25 MPa . In terms of the impact on the nucleation size, the two additional values of the normal stress are, respectively, equivalent to $D_c = 2$ and $1 \mu\text{m}$. Whereas decreasing D_c to 1 or $2 \mu\text{m}$ proportionally decreases the critical period T_a (Fig. 13), increasing σ to either 12.5 or even 25 MPa does not have any systematic effect on T_a . It is possible that the prefactor κ in the expression (24) of T_a slightly depends on σ , but

this dependence would be of lesser amplitude than the dependence of T_a on D_c/V_{pl} .

6 STEP RESPONSE OF A RATE-AND-STATE SEISMOGENIC FAULT

If the response of the seismicity to a shear stress history $\tau(t)$ applied on the fault were linear with the stress rate, the corresponding seismicity rate on the fault $R(t)$ could be written as a simple convolution:

$$R(t) = \mathcal{G}(t) * \dot{\tau}(t), \quad (26)$$

where the Green's function $\mathcal{G}(t)$ would be the response of the seismicity to a Dirac function for the stress rate, that is to a step function in stress. In other words, $\mathcal{G}(t)$ would simply be the seismicity rate of an aftershock sequence following a stress step of unit amplitude.

In this section, we therefore examine the response of the finite fault to a step-like perturbation in stress, and see to which extent it compares with the harmonic response of the fault described in the previous section. We do not study the step response in as much detail as the harmonic response. The goal of this section is to highlight some of the inherent properties of the finite fault revealed in the previous section and to illustrate the non-linearity of the response of the fault to stress perturbations.

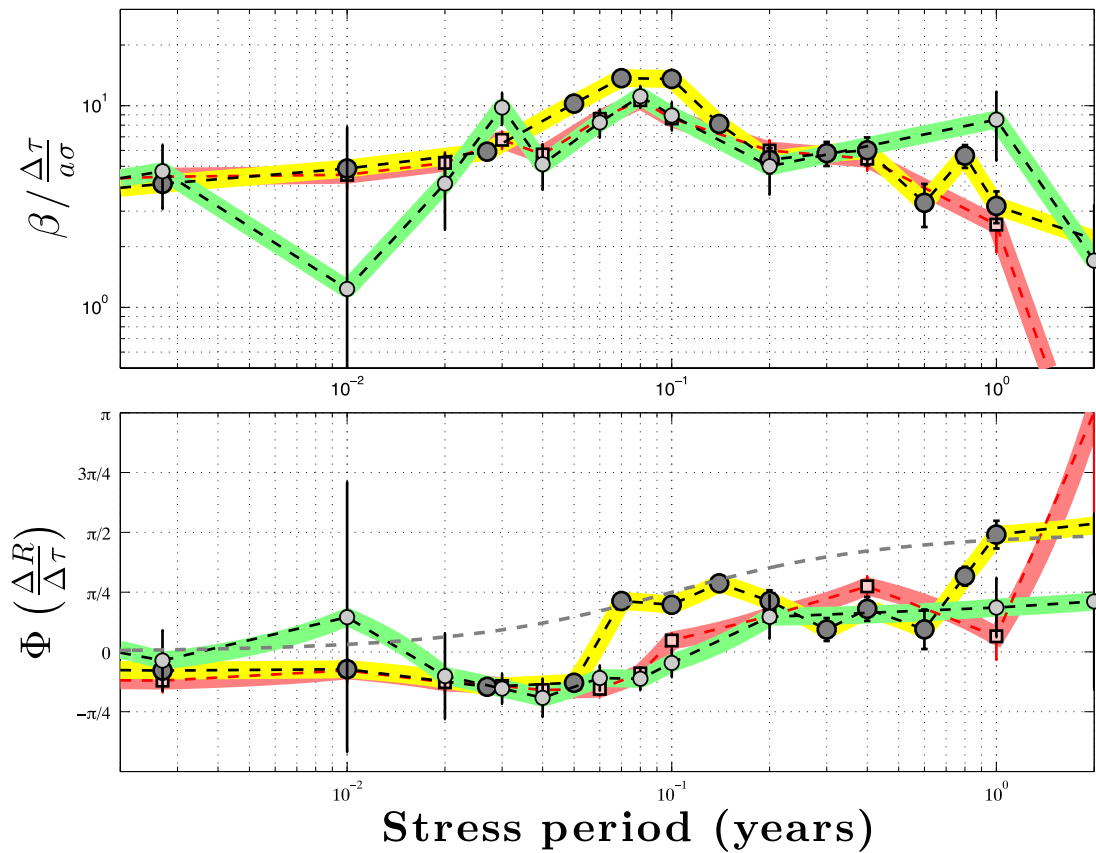


Figure 15. Response of a finite rate-and-state fault to harmonic shear-stress perturbations for three different values of the normal stress σ , for events rupturing the whole seismogenic patch. Large dark grey circles with yellow line: $\sigma = 5$ MPa, pink squares with the red line: $\sigma = 12.5$ MPa, small light grey circles with green line: $\sigma = 25$ MPa. The last two values of σ are, respectively, equivalent to $D_c = 2 \mu\text{m}$ (pink squares with the red line in Fig. 13) and $D_c = 1 \mu\text{m}$ (small light grey circles with green line in Fig. 13) in terms of changing the nucleation size and the size of the cohesive zone. As for the simulation in Fig. 13, the grid size has been changed accordingly. Unlike D_c , the normal stress does not change the position of the critical period T_a .

In order to determine the response of a finite fault to a step-like perturbation of stress, we consider the fault presented in Section 4 and alternately impose steps of shear stress of amplitude $\Delta\tau = 40$ kPa and -40 kPa so that $|\Delta\tau/a\sigma| = 1$. With this mode of perturbation, the mean of the stress perturbation is zero in the long term, so that no shear stress accumulates on the fault. As in the previous section, the fault is loaded at three different plate velocities: $V_{pl} = 0.1, 1$ and 10 cm yr^{-1} . When the fault is loaded at $V_{pl} = 0.1 \text{ cm yr}^{-1}$, the stress steps are applied every 50 yr, whereas they are applied every 5 yr when $V_{pl} = 1$ or 10 cm yr^{-1} . These time intervals are chosen because they are much longer than the characteristic time of response of the seismicity to a stress perturbation (e.g. Fig. 12), so that the transitory response of the seismicity to the step is over when the next step is imposed on the fault. Besides, Fig. 5 shows that 5 yr does not correspond to any natural periodicity of the fault loaded at $V_{pl} = 1 \text{ cm yr}^{-1}$, so that the steps happen at random times within the recurrence of the characteristic events of the fault. This remains true for the two other loading velocities studied ($V_{pl} = 0.1$ and 10 cm yr^{-1}). This can also be verified a posteriori by checking that the distribution of the time intervals between the last event and the stress step has an exponential distribution (see Fig. S5 for the case $V_{pl} = 1 \text{ cm yr}^{-1}$).

Given that the stress steps are imposed at random times during the interseismic period, in order to study the response of a population of faults that would be at different stages of their interseismic period, we stack the timing of events happening around the positive stress

steps, taking the time of the stress step as time zero. In the case of the fault loaded at $V_{pl} = 1 \text{ cm yr}^{-1}$, we select events happening between 0.2 yr before and 1 yr after the stress step is imposed. This time window is multiplied or divided by 10 when V_{pl} is, respectively, divided or multiplied by 10. It has been chosen in view of the results of the frequency response of the fault, where we determined that the characteristic period was of the order of $T_a = 2\pi t_a \approx 0.1 \text{ yr}$ (Fig. 12), which would correspond to a characteristic time of response to a stress-step perturbation of $t_a \approx 0.02 \text{ yr}$.

As described in Section 3, the SRM by Dieterich (1994) determines the cumulative number of events in response to a step of shear stress happening at time $t = 0$ for a spring-slider model under rate-and-state rheology. Similarly as in the case of the response to a harmonic variations of stress, we fit the cumulative number of events produced by the finite fault with an expression analogous to the prediction of the SRM (eq. 6):

$$\frac{N(t)}{r} = t + t_a \ln [e^\beta + (1 - e^\beta) e^{-t/t_a}] \mathcal{H}(t), \quad (27)$$

where the parameters β and t_a are determined to fit the results of the simulation. In the SRM, eq. (6) indicates that $\beta_{\text{SRM}} = \Delta\tau/a\sigma$ and $t_a|_{\text{SRM}} = a\sigma/\dot{\tau}_a$. Besides, according to eq. (27), the total number of events in the aftershock sequence is:

$$\frac{N_a}{r} = \beta t_a, \quad (28)$$

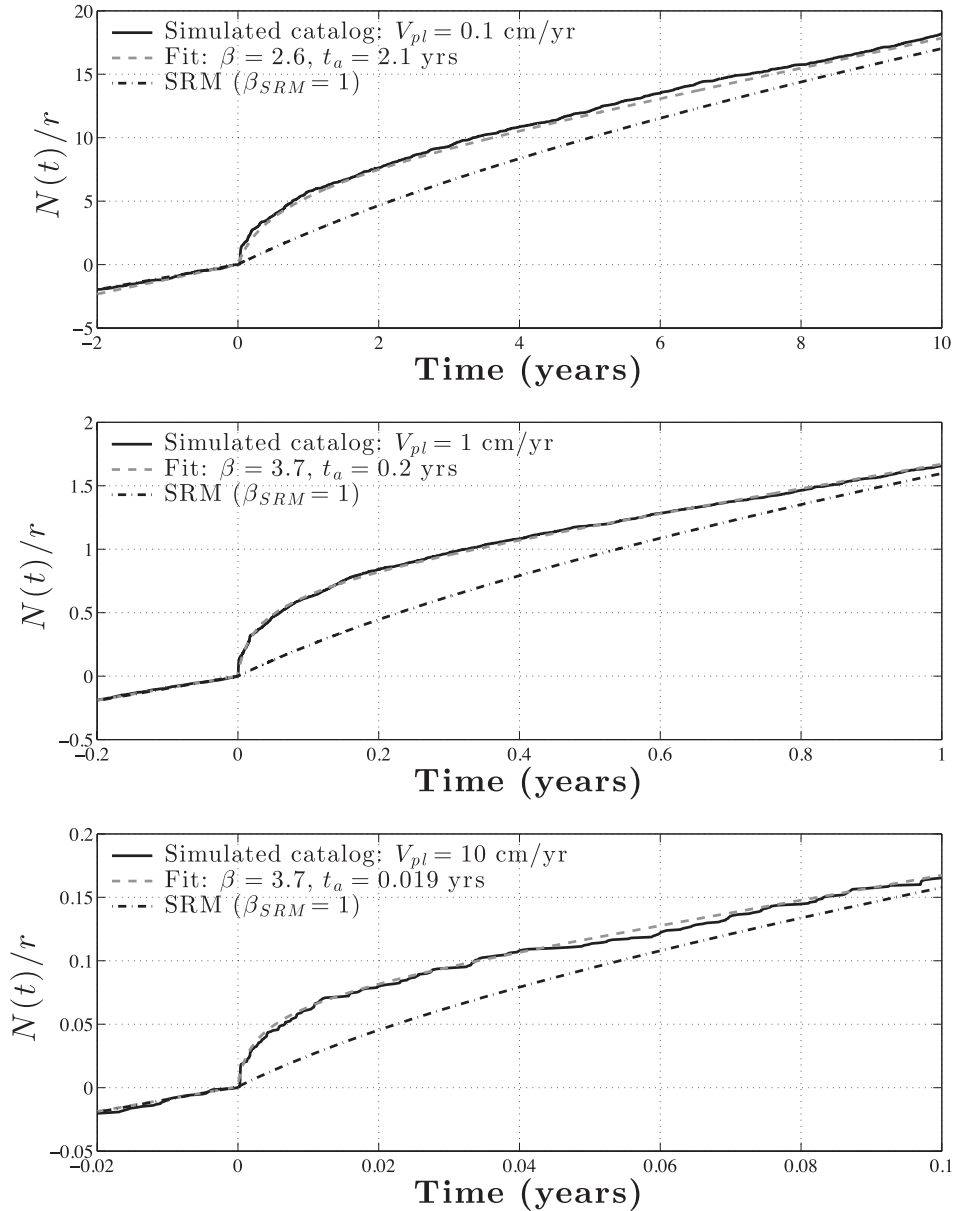


Figure 16. Cumulative number of events with time in response to a step of shear stress of amplitude $\Delta\tau/\sigma = 1$ at time $t = 0$, for three values of the loading rate ($V_{pl} = 0.1, 1$ and 10 cm yr^{-1}). The other parameters of the simulations are the same as in Section 4. Black curves show the cumulative number of events from the simulation, the dashed dark-grey curve shows the fit of eq. (27) to the cumulative distribution of events, where parameters r , t_a and β are determined to fit the results of the simulations. The dot-dashed black curve shows the fit with eq. (27) imposing the β -value prescribed by the SRM (i.e. $\beta_{SRM} = 1$ in this case) and fitting for the best value of t_a . Note that the ranges plotted on both axes are scaled by a factor proportional to $1/V_{pl}$. As for the harmonic response, the equation predicted by the SRM qualitatively fits the response of the finite fault, but underestimates the amplitude of the response (parameter β).

which in the case of the SRM simplifies to

$$\left. \frac{N_a}{r} \right|_{SRM} = \frac{\Delta\tau}{\dot{\tau}_a}. \quad (29)$$

Fig. 16 shows the cumulative number of events before and after the stress step is imposed (black curve), where the ranges plotted on the axes have been scaled by a factor inversely proportional to V_{pl} . The figure also shows the fit of eq. (27) to the cumulative number of events using β as a free parameter (dashed dark-grey curve), or imposing the value $\beta = \beta_{SRM} = \Delta\tau/\sigma = 1$ (dashed light-grey curve). Similarly to the case of the response to a harmonic stress perturbation, the SRM qualitatively reproduces the behaviour of the finite fault but underestimates the amplitude of the response.

In other words, eq. (27) fits well the cumulative seismicity rate in Fig. 16, but the best-fit value of β is much larger than what the SRM would predict. Imposing $\beta = \beta_{SRM} = \Delta\tau/\sigma$ as prescribed by the SRM and solving only for t_a never leads to a good fit (the best fitting curve with β_{SRM} is the dashed light-grey curve in Fig. 16).

The value of t_a obtained from the fit of eq. (27) to the cumulative number of events in the aftershock sequence generated with the finite-fault simulations ($t_a = 0.2 \text{ yr}$ in the case $V_{pl} = 1 \text{ cm yr}^{-1}$) is 10 times larger than the one computed in the case of the harmonic response ($t_a = 0.01 \text{ yr}$). This points out the non-linearity of the response of a fault to a stress perturbation, and therefore the challenge underlying the quest for a general simple law linking the stress history on a fault and the resulting seismicity rate.

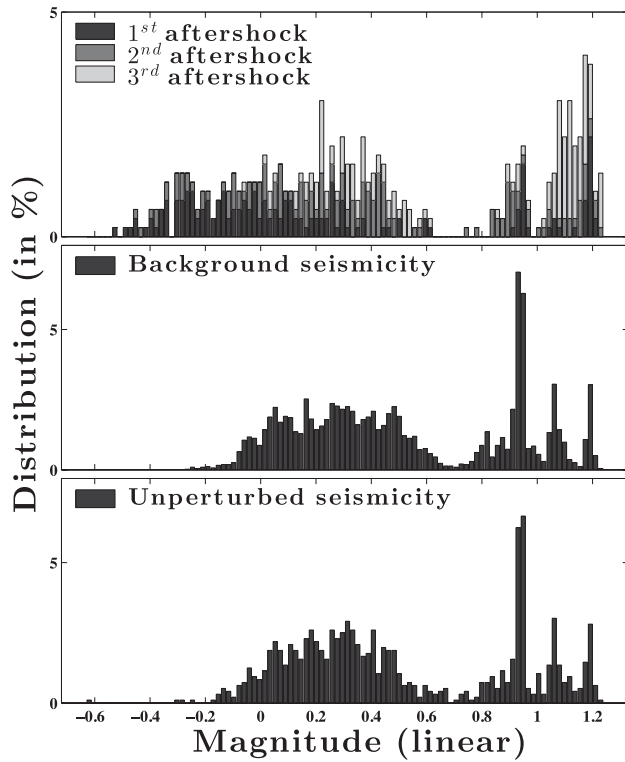


Figure 17. Magnitude distribution of: (top) the first three aftershocks after the fault undergoes a stress step; (middle) the background seismicity, that is, the seismicity starting 1 yr after the stress step has been applied, a time long enough for the stress step not to have any effect anymore; and (bottom) events from the unperturbed catalogue. The fault has the same properties as in Fig. 16, and it is loaded at $V_{pl} = 1 \text{ cm yr}^{-1}$. As for the response to a harmonic perturbation, the seismicity on the fault perturbed by a stress step is quite different from the one generated by the fault evolving unperturbed.

The characteristic time of response of the seismicity t_a is found to be inversely proportional to the loading velocity V_{pl} (Fig. 16), as in the case of the response to a harmonic perturbation and as predicted by the SRM. This finding also concurs with the observations of Toda *et al.* (2002), who reported that the characteristic duration of aftershock sequences in the Izu islands had decreased by a factor ~ 1000 during dyke intrusions that increased the background stressing rate by a factor ~ 1000 . Furthermore, as for the response to a harmonic perturbation, varying V_{pl} has an impact on the amplitude β of the response. However, the relation between amplitude β and background velocity V_{pl} seems different in both cases: the amplitude β of the response here appears to increase when V_{pl} increases, whereas β decreases when V_{pl} increases in the harmonic response. This points out another non-linearity of the response of the fault to stress perturbations, indicating that looking for a linear relation such as the one described in eq. (26) would be bound to fail.

Recall that in the case of the periodic perturbation, the magnitude distribution of events is different in the unperturbed and perturbed cases. Let us explore this phenomenon here. Fig. 17 shows the distribution of magnitudes of the first three aftershocks happening after each stress step, together with the magnitudes of the background seismicity on the same fault and the magnitudes of events produced by an unperturbed fault, in the case of $V_{pl} = 1 \text{ cm yr}^{-1}$. The background seismicity is defined here as the seismicity between 1 and 4 yr after the stress step has been applied on the fault (recall that the stress steps are applied every 5 yr), a time window chosen so that the

effect of the stress step has died off. As expected, the background seismicity on the perturbed fault is the same as the seismicity on the unperturbed fault, but aftershocks induced by the stress step have a different distribution of magnitudes. Some of these aftershocks have much smaller magnitudes than the unperturbed fault can produce (magnitudes between -0.6 and -0.2), while conversely, the proportion of aftershocks of magnitude $M_{lin} > 1$ is higher than the number of $M_{lin} > 1$ events on the unperturbed fault. It is noteworthy that while applying a step-like stress perturbation or a harmonic stress perturbation causes a change in the distribution of magnitudes produced by the fault, applying a random stress perturbation on the fault does not modify the type of events produced (Fig. S6).

The results of the step response of the finite fault are thus quite similar to the ones for the harmonic response, and lead again to the major conclusion that the finite fault is much more sensitive to stress perturbations than the SRM predicts.

7 DISCUSSION

7.1 High sensitivity of finite faults to stress perturbations

Our finite-faults study shows that seismicity is more sensitive to both harmonic and step-like stress perturbations than the predictions of the one-degree-of-freedom SRM of Dieterich (1994). The higher sensitivity of finite faults to the step-like perturbations has already been pointed out by Kaneko & Lapusta (2008). For the harmonic perturbations, the amplitude of the perturbed response is typically higher at all periods for the finite faults in comparison to the SRM, but the difference is especially high for the maximum-response period T_a , for which the amplification ranges from 10 to up to 1000 times, creating a peaked response at the period of T_a and potentially explaining the observations in Nepal.

Why does this difference arise? We propose that this effect is due to a combination of several factors which are clearly different between the finite-fault and SRM behaviours.

First, the characteristic evolution (often acceleration) of slip velocity in the nucleation zone is different on finite faults and in the spring-slider SRM model. For example, slip velocity is always increasing during nucleation in a spring-slider model under steady tectonic loading. On finite faults, the slip velocity is not necessarily monotonically increasing even in the unperturbed case, where it can decrease right before dramatically accelerating to inertially controlled instability (e.g. times between 5.16 and 5.2 yr in Fig. S3). The equations of SRM are essentially based on determining how the stress perturbation affects the slip velocity during the nucleation process. Hence SRM results are affected by choosing to analyse the slip-velocity evolution from the spring-slider model obtained analytically based on an assumption that $V\theta/D_c \gg 1$ throughout the nucleation process. As shown by Rubin & Ampuero (2005), a finite-fault nucleation zone with the aging form of the state variable evolution (also assumed in the SRM) and typical rate-and-state parameters has $V\theta/D_c = 1$ for most points and times during nucleation. This is just one indication that the evolution of a finite-fault nucleation zone is different. As shown by Kaneko & Lapusta (2008), this difference causes the finite-fault nucleation zones to react more strongly to stress-step perturbations, resulting in higher seismicity rates. The higher seismicity rates of Kaneko & Lapusta (2008) can be approximately explained if the true variation of slip velocity in the nucleation zone, computed numerically, is used in the Dieterich (1994) analysis instead of the one from the spring-slider model (section 7 of Kaneko & Lapusta 2008). The study of Kaneko & Lapusta (2008) also shows that an approximate analytical

solution for slip velocity in the finite nucleation zone from Rubin & Ampuero (2005), when used in the Dieterich (1994) analysis, explains a significant part (but not all) of their increased aftershock rates (appendix D3.2 of Kaneko & Lapusta 2008). Similar results hold for the slip law of the state-variable evolution (Kaneko and Lapusta, unpublished). Repeating the full analysis of Kaneko & Lapusta (2008) for harmonic perturbations is beyond the scope of this study. However, since our fault models are similar to the ones considered in Kaneko & Lapusta (2008), their finding that the enhanced sensitivity of the finite-fault to stress perturbations is due to the different slip-rate evolution in the nucleation zone than that of the SRM likely explains the large part of our results as well.

Second, the changes in earthquake sequences on the finite fault go much beyond the changes in times to instability for a single instance of a nucleation process, as assumed in the SRM model of Dieterich (1994) (as well as in Kaneko & Lapusta (2008)). In our study, the magnitude distribution of events on the perturbed faults substantially changes, perhaps not surprisingly for the ever-present harmonic perturbation that mimics the effect of seasonal variations or tides. Once even a single event of a different size occurs, it changes the prestress for all the following events, in addition to further effects of the constant harmonic variations. Hence, subsequent events are also bound to be different, including the conditions at the nucleation locations prior to each nucleation event. While this is clearly a difference between our finite-fault simulations and the formulation of the SRM, whether and how this difference contributes to the higher sensitivity of finite faults to harmonic perturbations requires further study.

Third, the nucleation on finite faults occurs in an expanding zone with complex temporal and spatial variations (e.g. Figs. S2–S3). Different points within the nucleation zone have different slip-rate evolutions, and their interaction determines the overall acceleration of the nucleation zone to a seismic event. For example, as shown by Kaneko & Lapusta (2008), positive stress steps, which always advance the time to instability in spring-slider models, can actually postpone the subsequent seismic event on a finite fault. This is because the stress step can accelerate the nucleation zone to an aseismic transient, which relieves stress in the nucleation zone and requires longer subsequent loading to achieve seismic sliding. Such complex space-dependent slip interactions cannot occur in a single-degree-of-freedom SRM. With the addition of harmonic stress perturbations, both the slip rate of individual points as well as the advancement of the nucleation zone tip into the locked seismogenic zone becomes even more complex and of oscillatory nature. Understanding how the nucleation zone grows under the influence of a stress perturbation is therefore a prerequisite for the establishment of an analytical framework describing the correlation of the timing of events with a given stress history in terms of the model parameters. A promising approach would be to extend the study of Rubin & Ampuero (2005), which shows that nucleation processes on uniformly prestressed and steadily loaded rate-and-state faults with the aging form of the state variable evolution can be approximated as quasi-statically expanding cracks. For such cracks, the expansion is governed by the balance of the energy dissipated at the crack tip (often called the fracture or breakdown energy) and the elastic energy released as crack advances. For the unperturbed faults, the breakdown energy grows as the crack-like nucleation zone expands, with a logarithmic dependence on the characteristic slip rate, and the elastic-energy release per unit crack advance also grows, as it scales with $l\Delta\tau^2$, where l is the (expanding) nucleation zone length and $\Delta\tau$ is the average difference between the prestress before the nucleation and the (approximately constant) friction in

the middle of the expanding nucleation zone. In the presence of harmonic oscillations, both the breakdown energy and elastic energy released will acquire a history-dependent oscillatory component. The detailed study of that behaviour, which is beyond the scope of this paper, may be quite revealing in terms of the dependence of the nucleation size and timing on the period and phase of the perturbation.

As mentioned in Section 5.3, basing their study on the behaviour of a spring-slider system with rate-weakening rheology, Perfettini *et al.* (2001) demonstrated the possibility of a resonance of the slip rate in the nucleation zone with a harmonic perturbation of normal or shear stress at the critical period $T_c = 2\pi\sqrt{a/(b-a)}(D_c/V_N)$, where V_N is the loading velocity on the slider. The assumption of Perfettini *et al.* (2001) that $V\theta/D_c = 1$ is close to what occurs in our finite-fault nucleation zones, where points away from the tips of the zone are in nearly steady sliding (Fig. S3). If we take the range of the steady-state velocities in the nucleation zone observed in our simulations, $V = 0.04\text{--}0.2\text{ cm yr}^{-1}$ (Fig. S3) as the estimate of V_N , then the value of T_c is estimated to range between 0.02 and 0.1 yr, close to the value of $T_a = 0.03\text{ yr}$ (Fig. 7). However, as shown in Perfettini *et al.* (2001), the resonance would have a noticeable effect only for perturbing periods T within 5 per cent of T_c . In the finite-fault simulations in our study, the increase of correlation is noticeable at periods at least 4 orders of magnitude around the critical period T_a (Fig. 7). Therefore, the resonance phenomenon likely explains a part of the high correlation around T_a , but cannot alone explain the higher sensitivity of the finite fault to stress perturbations at all periods. This again points to the differences between the nucleation-zone processes and their perturbed behaviour in finite-fault and spring-slider models, as already discussed.

There have been other findings potentially relevant to explaining the response of finite faults to harmonic stress perturbations. Ader *et al.* (2012) showed that the amplitude of slip-rate variations of a spring-slider system with rate-strengthening rheology under harmonic stress perturbations can be period-dependent at periods $T < T_a$. In their study, the period dependence comes from the following findings. If the period T of the perturbation is smaller than the period $T_\theta = 2\pi\theta_{ss} = 2\pi D_c/V_{ss}$, where θ_{ss} is the steady-state value of the state variable, and also the characteristic time for the state-variable evolution, and V_{ss} is the steady-state slip rate, the amplitude of the slip-rate variations is $\Delta V/V_{ss} = \Delta\tau/a\sigma$. However, when $T > T_\theta$, then $\Delta V/V_{ss} = \Delta\tau/(a-b)\sigma$. Therefore, the rate-strengthening part of the finite fault has a period-dependent variation in its slip rate, which may create a period-dependent stressing on the nearby rate-weakening segment where seismic events nucleate. However, such effect appears to be too small to be responsible for the period-dependent response of the seismogenic patch in our study. It is difficult to isolate the various contributions to oscillations in the stressing rate on the rate-weakening part of the fault. But we can judge the importance of such rate-strengthening zone effect by varying it and observing the corresponding variations in the seismicity response. Fig. S9 shows the response of the finite fault where we have imposed $b = 0$ in the rate-strengthening areas of the fault, so that the response of the rate-strengthening areas is not period-dependent any more since $a - b = a$. It is clear that such a modification does not alter the period-dependent response of the seismicity. Moreover, no noticeable stress amplification in any part of the rate-weakening zone, due to oscillations of the creep in the rate-strengthening zone, has been detected (Fig. S10). Hence we conclude that the period dependence in the rate-strengthening regions does not have a noticeable effect on the enhanced seismicity response in our finite-fault models, as expected for the values of

$\Delta\tau/a\sigma$ and $\Delta\tau/(a-b)\sigma$ considered in this study which are small compared to 1.

7.2 Implications for the estimation of $a\sigma$

A recurring feature in the behaviour of a finite fault undergoing a stress perturbation in our study is that the amplitude of the response is much larger than the predictions of the SRM. This observation calls for caution regarding the estimates of $a\sigma$ computed from the response of seismicity to stress perturbations, which are usually based on the predictions of the SRM (Gross & Kisslinger 1997; Gross & Bürgmann 1998; Toda *et al.* 1998; Cochran *et al.* 2004; Bettinelli *et al.* 2008; Toda *et al.* 2012).

In order to compute $a\sigma$, one generally estimates the amplitude β of the relative variations of seismicity rate in response to a stress perturbation. In the case of periodic variations, β is half the peak-to-peak value of the seismicity rate, whereas for an aftershock sequence, a fit of eq. (27) to the cumulative number of events is necessary to estimate β . Considering that this amplitude can be expressed as a function of the problem parameters with the predictions of the SRM, $a\sigma = \Delta\tau/\beta$, where the amplitude $\Delta\tau$ of the perturbation can be evaluated provided the fault geometry at the location of the events considered.

However, the finite-fault simulations indicate that the amplitude of the response is larger than the predictions of the SRM, so that it may be possible to observe a strong response of the seismicity to a shear stress perturbation without necessarily requiring very small values of $a\sigma$.

In the case where the finite fault is subjected to harmonic stress perturbations, the amplitude of the response at $T = 0.0027$ yr is five times larger than what would be predicted by the SRM. This cannot be due to a resonance with the return period of events on the fault, as $T = 0.0027$ yr is two orders of magnitude less than the natural periodicities on the fault (Fig. 5). At $T = 0.027$ yr, the amplitude of the response is about 20 times larger than the predictions of the SRM. As a result, using the SRM to explain the large amplitude of the seismicity-rate variations at $T = 0.027$ yr, knowing that the perturbation has a $\Delta\tau = 3$ kPa amplitude yields $a\sigma \approx 2$ kPa, where in fact $a\sigma = 40$ kPa, an underestimation by an order of magnitude.

Such an underestimation could have important implications for values of $a\sigma$ that have been estimated for real faults from their response to a periodic perturbation (Cochran *et al.* 2004; Bettinelli *et al.* 2008). The actual value of $a\sigma$ in the seismogenic zone may actually be an order of magnitude larger than the value computed with the SRM, which would then allow the effective normal stress to be closer to the overburden minus hydrostatic pore pressure at seismogenic depths, at places where aftershocks occur.

The same conclusions remain true when estimating $a\sigma$ from aftershock sequences with the SRM predictions (Gross & Kisslinger 1997; Gross & Bürgmann 1998; Toda *et al.* 1998, 2012). Gross & Kisslinger (1997) and Gross & Bürgmann (1998) actually used the total number of aftershocks N_a to first estimate $\dot{\tau}_a$ from the predictions of the SRM with eq. (29) and then to obtain t_a from the fit of eq. (27) to the cumulative number of events, to finally estimate $a\sigma = t_a \dot{\tau}_a$. This procedure is equivalent to estimating $a\sigma = \Delta\tau/\beta$ from the β -value from the fit. As our finite-fault simulations show, the observed value of β is greater than the predictions from the SRM, which would lead to underestimating $a\sigma$, as in the case of the harmonic response. Similar issues with estimating $a\sigma$ from stress-step observations using the spring-slider-based SRM equations have been pointed out by Kaneko & Lapusta (2008) for a different finite-fault problem.

8 CONCLUSIONS

We consider the response of a continuum model with a finite seismogenic patch of rate-weakening rate-and-state rheology surrounded by rate-strengthening, creeping areas subjected to a stress perturbation. Our main findings are (1) the much higher amplitudes of the seismicity response than predicted by the spring-slider-based SRM model by Dieterich (1994) and (2) the peaked nature of the response at a critical period which we denote by T_a , unlike the response of the SRM which is monotonic. These findings may explain why the seismicity response to seasonal variations in Nepal is more prominent than that to tidal variations, even though both stress perturbations have comparable amplitude (Bettinelli *et al.* 2008; Ader & Avouac 2013). The important factor is the difference in periods, 1 yr versus several hours. If the properties of the perturbed faults are such that T_a is close to 1 yr, a value that is achievable for reasonable rate-and-state properties in our simulations, then our models indeed predict that the response to seasonal variations could be much more prominent, by a factor of 10–1000. Our findings can also explain similar observations for experimental faults (Lockner & Beeler 1999; Beeler & Lockner 2003).

Nevertheless, the finite-fault response in our study has features similar to the SRM model of Dieterich (1994). The qualitative shape of the seismicity rate in response to either a harmonic stress perturbation or a stress step can be approximately fit by the predictions of the SRM if one treats the amplitude of the response as a fitting parameter; the difference we find is that the amplitudes needed for a good fit are higher than the ones predicted by the SRM model. In the case of the harmonic response, the seismicity rate on the finite faults in our study is approximately in phase with the stress perturbation at periods shorter than the critical period T_a , and in phase with the stress rate at periods larger than T_a , in agreement with the predictions of the SRM. The expression (24) for T_a derived based on the corresponding separating period of the SRM results in dependencies of T_a on model parameters that can be verified for the finite faults through simulations. In particular, we find that T_a is proportional to the characteristic rate-and-state slip D_c , inversely proportional to the secular loading velocity V_{pl} , and independent of the effective normal stress σ .

One factor of significant differences we find between the finite-fault and SRM response to perturbations is the spatial variation of stress and slip and the resulting space-based stress transfers and slip interactions. As a result, nucleation processes, which are the key time-dependent features that allow rate-and-state models to reproduce the observed time-dependent decay of aftershock sequences, proceed quite differently on finite faults in comparison with SRM model assumptions. Finite faults feature an expanding nucleation zone within the rate-weakening patch (which cannot exist in the one degree of freedom SRM) and experience the corresponding quite different evolution of the characteristic slip rate within the nucleation zone (Rubin & Ampuero 2005; Kaneko & Lapusta 2008). In particular, the SRM assumption that $V\theta/D_c \gg 1$ during nucleation is violated in most inner points of the expanding finite-fault nucleation zone, where $V\theta/D_c \approx 1$, corresponding to steady sliding. Note that the corresponding difference in slip-rate evolution between the finite-fault and SRM nucleation was used to explain the finding of higher seismicity response on finite faults in a study of stress-step perturbations by Kaneko & Lapusta (2008). Moreover, a study of Perfettini *et al.* (2001), which considered the response to periodic stress perturbations of a spring-slider system in steady sliding ($V\theta/D_c = 1$), found resonance-like responses which are absent in the SRM but present in our finite-fault study.

These findings imply that the nature of the characteristic slip-velocity evolution, and perhaps expansion, of the nucleation zone is of paramount importance to its response to stress perturbations, and future work should be directed towards constructing analytical approximations of the nucleation behaviour observed in finite-fault simulations, as done in Rubin & Ampuero (2005) for a different problem (one of the nucleation size on an unperturbed fault).

Another important difference between the finite-fault response in our study and the SRM methodology is in the nature of the perturbed events. In the SRM, a single nucleation process is considered, and the altered seismicity response comes from the advance or delay of the time to instability of that nucleation process in response to stress perturbations. However, in our finite-fault models, the entire sequence of events is modified on the perturbed faults, with nucleation processes proceeding under modified prestress conditions compared with the unperturbed faults. The magnitude distribution of events on the perturbed fault is also substantially altered, with different ranges of magnitudes, and a different balance between larger and smaller events. Note that the seismicity patterns on the perturbed faults can be either more or less complex than those on the unperturbed faults. In some cases, perturbations result in a larger fraction of smaller events that rupture only a part of the seismogenic patch, and in other cases, perturbations decrease the number of such smaller events. The typical larger events that span the entire seismogenic patch are also affected by perturbations, changing their magnitude and typical recurrence time. Hence the perturbed events are not simply the time-advanced or delayed versions of the unperturbed events, they are different events. In retrospect, this should not be surprising. In the finite-fault models, the rupture initiates when the nucleation zone reaches a critical size, and the distribution of stresses on the fault at that instance determines how far the rupture propagates, that is the size of the event. The timing of the event is thus directly linked to the growth process of the nucleation zone, which is quite sensitive to stress perturbations. When the modified nucleation process is over, the pre-stresses further along the fault are different from what they would have been on the unperturbed fault. The difference in prestress modifies the size of the resulting event, which in turn affects the pre-stress for subsequent events.

Our finite-fault simulations yield two regimes, with the seismicity variations being either in-phase or out-of-phase with the stress perturbation, as the SRM model also predicts, separated by a critical period T_a . The value of the peak response at that period, which is much larger than what the SRM model predicts, is however more difficult to explain. Unlike in the SRM, V_{pl} and D_c have an effect on the amplitude of the response. In the case of V_{pl} , the effect is opposite for the responses to harmonic and step-like perturbations: increasing V_{pl} increases the amplitude of the response to a stress step whereas it decreases the amplitude of the response to a harmonic perturbation at the critical period T_a . This is another illustration of the non-linearity of the response of the finite faults. In the case of harmonic perturbations, varying V_{pl} can modify the amplitude of the response by several orders of magnitude. Similarly, increasing the characteristic distance D_c makes the finite fault more sensitive to harmonic stress perturbations at the characteristic period T_a . The reasons for these dependences need to be further investigated.

Our findings advance the possibility of determining fault friction properties based on observations of perturbed seismicity. The enhanced response to perturbations in the finite-fault models indicates that values of the product $a\sigma$ obtained from observations based on the comparisons with the SRM model are likely to be underestimated, by as much as one to two orders of magnitude, as discussed in Section 7.2. Our results could also be used to explain the be-

haviour of the seismicity in Nepal, implying that $T_a \approx 1$ yr for the natural faults in the area and giving a constraint on the acceptable sets of fault properties.

ACKNOWLEDGEMENTS

This project was supported by the Gordon and Betty Moore Foundation, through the Tectonics Observatory, NSF grant EAR #0838495. This is Caltech Tectonic Observatory's contribution number 231 and Caltech Seismolab contribution number 10093.

REFERENCES

- Ader, T. & Avouac, J.-P., 2013. Detecting periodicities in earthquake catalogs using the Schuster test, application to Himalayan seismicity, *Earth planet. Sci. Lett.*, **377–378**, 97–105.
- Ader, T., Ampuero, J.-P. & Avouac, J.-P., 2012. The role of velocity-neutral creep on the modulation of tectonic tremor activity by periodic loading, *Geophys. Res. Lett.*, **39**, L16310, doi:10.1029/2012GL052326.
- Barbot, S., Fialko, Y. & Bock, Y., 2009. Postseismic deformation due to the M_w 6.0 2004 Parkfield earthquake: Stress-driven creep on a fault with spatially variable rate-and-state friction parameters, *J. geophys. Res.*, **114**, B07405, doi:10.1029/2008JB005748.
- Beeler, N.M. & Lockner, D.A., 2003. Why earthquakes correlate weakly with the solid Earth tides: effects of periodic stress on the rate and probability of earthquake occurrence, *J. geophys. Res.*, **108**(B8), 2391, doi:10.1029/2001JB001518.
- Bettinelli, P., Avouac, J.-P., Flouzat, M., Bollinger, L., Ramillien, G., Rajaure, S. & Sapkota, S., 2008. Seasonal variations of seismicity and geodetic strain in the Himalaya induced by surface hydrology, *Earth planet. Sci. Lett.*, **266**, 332–344.
- Bollinger, L., Perrier, F., Avouac, J.-P., Sapkota, S. & Gautam, U.T.D.R., 2007. Seasonal modulation of seismicity in the Himalaya of Nepal, *Geophys. Res. Lett.*, **34**, L08304, doi:10.1029/2006GL029192.
- Bosl, W.J. & Nur, A., 2002. Aftershocks and pore fluid diffusion following the 1992 Landers earthquake, *J. geophys. Res.*, **107**(B12), 2366, doi:10.1029/2001JB000155.
- Cappa, F., Rutqvist, J. & Yamamoto, K., 2009. Modeling crustal deformation and rupture processes related to upwelling of deep CO₂-rich fluids during the 1965–1967 Matsushiro earthquake swarm in Japan, *J. geophys. Res. - Solid Earth*, **114**, B10304, doi:10.1029/2009JB006398.
- Cattin, R. & Avouac, J., 2000. Modeling mountain building and the seismic cycle in the Himalaya of Nepal, *J. geophys. Res. - Solid Earth*, **105**, 13 389–13 407.
- Christiansen, L., Hurwitz, S., Saar, M., Ingebritsen, S. & Hsieh, P., 2005. Seasonal seismicity at western United States volcanic centers, *Earth planet. Sci. Lett.*, **240**, 307–321.
- Christiansen, L.B., Hurwitz, S. & Ingebritsen, S.E., 2007. Annual modulation of seismicity along the San Andreas Fault near Parkfield, CA, *Geophys. Res. Lett.*, **34**, L04306, doi:10.1029/2006GL028634.
- Cochran, E.S., Vidale, J.E. & Tanaka, S., 2004. Earth tides can trigger shallow thrust fault earthquakes, *Science*, **306**, 1164–1166.
- Dahm, T., Hainzl, S. & Fischer, T., 2010. Bidirectional and unidirectional fracture growth during hydrofracturing: role of driving stress gradients, *J. geophys. Res. - Solid Earth*, **115**, B12322, doi:10.1029/2009JB006817.
- Day, S.M., Dalguer, L.A., Lapusta, N. & Liu, Y., 2005. Comparison of finite difference and boundary integral solutions to three-dimensional spontaneous rupture, *J. geophys. Res.*, **110**, B12307, doi:10.1029/2005JB003813.
- Dieterich, J.H., 1978. Time-dependent friction and the mechanics of stick-slip, *Pure appl. Geophys.*, **116**, 790–806.
- Dieterich, J.H., 1979a. Modeling of rock friction 1: experimental results and constitutive equations, *J. geophys. Res.*, **84**, 2161–2168.
- Dieterich, J.H., 1979b. Modeling of rock friction 2: simulation of preseismic slip, *J. geophys. Res.*, **84**, 2169–2175.
- Dieterich, J.H., 1987. Nucleation and triggering of earthquake slip—effect of periodic stresses, *Tectonophysics*, **144**(1–3), 127–139.

- Dieterich, J.H., 1992. Earthquake nucleation on faults with rate and state-dependent friction, *Tectonophysics*, **211**, 115–134.
- Dieterich, J.H., 1994. A constitutive Law for rate of earthquakes production and its application to earthquake clustering, *J. geophys. Res.*, **99**(B2), 2601–2618.
- Dieterich, J.H., 2007. Applications of rate-and-state-dependent friction to models of fault slip and earthquake occurrence, *Treatise geophys.*, **4**, 107–129.
- Dieterich, J.H. & Kilgore, B.D., 1994. Direct observation of frictional contacts: new insights for state-dependent properties, *Pure appl. Geophys.*, **143**, 283–302.
- Felzer, K.R. & Brodsky, E.E., 2006. Decay of aftershock density with distance indicates triggering by dynamic stress, *Nat. Geosci.*, **441**, 735–738.
- Freund, L.B., 1990. *Dynamic Fracture Mechanics*, 1st edn, Cambridge Univ. Press.
- Fukuda, J., Johnson, K.M., Larson, K. & Miyazaki, S., 2009. Fault friction parameters inferred from the early stages of afterslip following the 2003 Tokachi-oki earthquake, *J. geophys. Res.*, **114**, B04412, doi:10.1029/2008JB006166.
- Gomberg, J., Bodin, P. & Reasenber, P.A., 2003. Observing earthquakes triggered in the near field by dynamic deformations, *Bull. seism. Soc. Am.*, **93**, 118–138.
- Gross, S. & Bürgmann, R., 1998. Rate and state of background stress estimated from the aftershocks of the 1989 Loma Prieta, California, earthquake, *J. geophys. Res.*, **103**(B3), 4915–4927.
- Gross, S. & Kisslinger, C., 1997. Estimating tectonic stress rate and state with Landers aftershocks, *J. geophys. Res.*, **102**(B4), 7603–7612.
- Hainzl, S. & Fischer, T., 2002. Indications for a successively triggered rupture growth underlying the 2000 earthquake swarm in Vogtland/NW Bohemia, *J. geophys. Res.-Solid Earth*, **107**(B12), 2338, doi:10.1029/2002JB001865.
- Hainzl, S., Kraft, T., Wassermann, J., Igel, H. & Schmedes, E., 2006. Evidence for rainfall-triggered earthquake activity, *Geophys. Res. Lett.*, **33**(19), doi:10.1029/2006GL027642.
- Hearn, E., Bürgmann, R. & Reilinger, R., 2002. Dynamics of Izmit earthquake postseismic deformation and loading of the Duzce earthquake hypocenter, *Bull. seism. Soc. Am.*, **92**, 172–193.
- Heki, K., 2003. Snow load and seasonal variation of earthquake occurrence in Japan, *Earth planet. Sci. Lett.*, **207**, 159–164.
- Hill, D.P., 1993. Seismicity remotely triggered by the magnitude 7.3 Landers, California, earthquake, *Science*, **260**, 1617–1623.
- Hsu, Y.-J., Simons, M., Avouac, J.-P., Galetzka, J., Sieh, K., Natawidjaja, C.M., Prawirodirdjo, D.L. & Bock, Y., 2006. Frictional afterslip following the Mw 8.7, 2005 Nias-Simeulue earthquake, Sumatra, *Science*, **312**, 1921–1926.
- Hsu, Y.-J., Yu, S.-B. & Chen, H.-Y., 2009a. Coseismic and postseismic deformation associated with the 2003 Chengkung, Taiwan, earthquake, *Geophys. J. Int.*, **176**(2), 420–430.
- Hsu, Y.-J., Avouac, J.-P., Yu, S.-B., Chang, C.-H., Wu, Y.-M. & Woessner, J., 2009b. Spatio-temporal Slip & Stress Level on the Faults within the Western Foothills of Taiwan: implications for Fault Frictional Properties, *Pure appl. Geophys.*, **166**, 1853–1884.
- Kaneko, Y. & Lapusta, N., 2008. Variability of earthquake nucleation in continuum models of rate-and-state faults and implications for aftershock rates, *J. geophys. Res.*, **113**, B12312, doi:10.1029/2007JB005154.
- Lapusta, N. & Liu, Y., 2009. Three-dimensional boundary integral modeling of spontaneous earthquake sequences and aseismic slip, *J. geophys. Res.*, **114**, B09303, doi:10.1029/2008JB005934.
- Lapusta, N. & Rice, J.R., 2003. Nucleation and early seismic propagation of small and large events in a crustal earthquake model, *J. geophys. Res.*, **108**(B4), 2205, doi:10.1029/2001JB000793.
- Lapusta, N., Rice, J.R., BenZion, G. & Zheng, G., 2000. Elastodynamic analysis for slow tectonic loading with spontaneous rupture episodes on faults with rate- and state-dependent friction, *J. geophys. Res.*, **105**, 23 765–23 789.
- Lockner, D. & Beeler, N., 1999. Premonitory slip and tidal triggering of earthquakes, *J. geophys. Res.-Solid Earth*, **104**(B9), 20 133–20 151.
- Marone, C., 1998. Laboratory-derived friction laws and their application to seismic faulting, *Ann. Revs. Earth planet. Sci.*, **26**, 643–696.
- Miyazaki, S., Segall, P., Fukuda, J. & Kato, T., 2004. Space time distribution of afterslip following the 2003 Tokachi-oki earthquake: implications for variations in fault zone frictional properties, *Geophys. Res. Lett.*, **31**, L06623, doi:10.1029/2003GL019410.
- Noda, H. & Lapusta, N., 2010. Three-dimensional earthquake sequence simulations with evolving temperature and pore pressure due to shear heating: effect of heterogeneous hydraulic diffusivity, *J. geophys. Res.*, **115**, B12314, doi:10.1029/2010JB007780.
- Nur, A. & Booker, J.R., 1972. Aftershocks caused by pore fluid flow?, *Science*, **175**, 885–887.
- Palmer, A.C. & Rice, J.R., 1973. The growth of slip surfaces in the progressive failure of overconsolidated clay slopes, *Proc. R. Soc. Lond.*, **332**, 527–548.
- Perfettini, H. & Avouac, J.-P., 2004. Postseismic relaxation driven by brittle creep: a possible mechanism to reconcile geodetic measurements and the decay rate of aftershocks, application to the Chi-Chi earthquake, Taiwan, *J. geophys. Res.*, **109**(B2), B02304, doi:10.1029/2003JB002488.
- Perfettini, H. & Avouac, J.-P., 2007. Modeling afterslip and aftershocks following the 1992 Landers earthquake, *J. geophys. Res.*, **112**, B07409, doi:10.1029/2006JB004399.
- Perfettini, H., Schmittbuhl, J., Rice, J.R. & Cocco, M., 2001. Frictional response induced by time-dependent fluctuations of the normal loading, *J. geophys. Res.*, **106**(B7), 13 455–13 472.
- Rice, J.R. & Ruina, A., 1983. Stability of steady frictional slipping, *J. appl. Mech.*, **50**, 343–349.
- Rubin, A.M. & Ampuero, J.-P., 2005. Earthquake nucleation on (aging) rate and state faults, *J. geophys. Res.*, **110**, B11312, doi:10.1029/2005JB003686.
- Ruina, A., 1983. Slip instability and state variable friction laws, *J. geophys. Res.*, **88**, 10 359–10 370.
- Saar, M.O. & Manga, M., 2003. Seismicity induced by seasonal groundwater recharge at Mt. Hood, Oregon, *Earth planet. Sci. Lett.*, **214**, 605–618.
- Savage, H.M. & Marone, C., 2007. Effects of shear velocity oscillations on stick-slip behavior in laboratory experiments, *J. geophys. Res.*, **112**, B02301, doi:10.1029/2005JB004238.
- Savage, H.M. & Marone, C., 2008. Potential for earthquake triggering from transient deformations, *J. geophys. Res.*, **113**, B05302, doi:10.1029/2007JB005277.
- Tanaka, S., Ohtake, M. & Sato, H., 2002. Evidence for tidal triggering of earthquakes as revealed from statistical analysis of global data, *J. geophys. Res.*, **107**, 2211, doi:10.1029/2001JB001577.
- Toda, S., Stein, R.S., Reasenber, P.A., Dieterich, J.H. & Yoshida, A., 1998. Stresstransferred by the 1995 $M_w = 6.9$ Kobe, Japan, shock: effect on aftershocks and future earthquake probabilities, *J. geophys. Res.*, **103**(B10), 24 543–24 565.
- Toda, S., Stein, R.S. & Sagiya, T., 2002. Evidence from the AD 2000 Izu islands earthquake swarm that stressing rate governs seismicity, *Nat. Geosci.*, **419**, 58–61.
- Toda, S., Stein, R.S., Beroza, G.C. & Marsan, D., 2012. Aftershocks halted by static stress shadows, *Nat. Geosci.*, **5**, 410–413.
- Utsu, T., Ogata, Y. & Matsu'ura, R.S., 2005. The centenary of the Omori formula for a decay law of aftershock activity, *J. Phys. Earth*, **43**, 1–33.
- Wilcock, W.S., 2001. Tidal triggering of microearthquakes on the Juan de Fuca Ridge, *Geophys. Res. Lett.*, **28**(20), 3999–4002.

APPENDIX A: RESPONSE OF SEISMICITY TO HARMONIC STRESS PERTURBATIONS IN THE COULOMB FAILURE MODEL

The CFM predicts that the seismicity rate on the fault should be proportional to the stressing rate. Calling r the seismicity rate on the fault under constant stressing rate $\dot{\tau}_a$, this implies that, under a

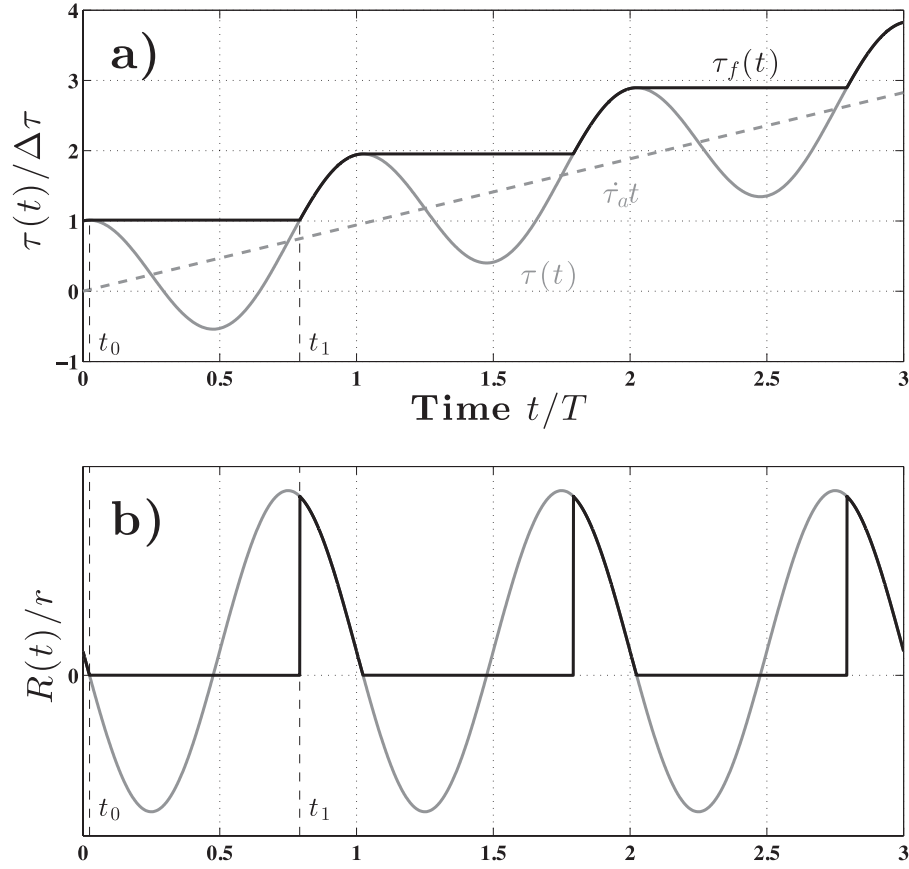


Figure A1. Evolution of the seismicity rate under a harmonic stress perturbation according to a Coulomb failure model (CFM). (a) Shear loading on the fault. The dashed grey line shows the secular loading $\dot{\tau}_a t$ on the fault, while the plain grey curve represents the total shear stress on the fault $\tau(t)$ (secular loading and harmonic variations). The black curve shows the stress actually ‘seen’ by the seismicity, that is the increasing envelope of the stress on the fault. (b) Seismicity rate on the fault corresponding to the shear stresses from upper plot. The grey curve shows the seismicity rate if it were truly proportional to the shear stress rate (and would thus be occasionally negative), while the black curve shows the actual (positive) seismicity rate on the fault. When the period of the stress becomes small enough, the actual amplitude of the seismicity-rate variations becomes smaller than that of the stress rate (black and grey curves on plot b, respectively).

stress history $\tau(t)$, a fault would have the following seismicity rate $R(t)$:

$$\frac{R(t)}{r} = \frac{\dot{\tau}(t)}{\dot{\tau}_a}. \quad (\text{A1})$$

This relation, however, is only true if the stresses on the faults are distributed uniformly up to the Coulomb failure stress (CFS). Also, the seismicity rate can clearly not have negative values. Therefore, if $\tau(t)$ decreases, the seismicity will shut off and only resume when the stress on the fault will have increased back to a value greater than its preceding largest value. Otherwise, all the faults that have not ruptured yet will have stresses less than the CFS. Calling $\tau_f(t)$ the non-decreasing envelope of $\tau(t)$ (Fig. A1), the seismicity rate on the fault should actually be written as:

$$\frac{R(t)}{r} = \frac{\dot{\tau}_f(t)}{\dot{\tau}_a}. \quad (\text{A2})$$

The stresses as well as the corresponding seismicity rate are represented in Fig. A1, for the case where the shear stress $\tau(t)$ decreases at some point.

For a stress history made of a component increasing at constant rate $\dot{\tau}_a$ and a harmonic variation of amplitude $\Delta\tau$ and period T ,

$$\tau(t) = \dot{\tau}_a t + \Delta\tau \cos\left(2\pi \frac{t}{T}\right), \quad (\text{A3})$$

the stress rate is increasing on the fault if $\dot{\tau}_a \geq 2\pi \Delta\tau/T$, that is

$$T \geq T_\tau = \frac{2\pi \Delta\tau}{\dot{\tau}_a}. \quad (\text{A4})$$

In this case, $\tau_f(t) = \tau(t)$ and the amplitude of the seismicity-rate variations is simply:

$$\frac{\Delta R}{r} = \frac{T_\tau}{T}, \quad (\text{A5})$$

so that, for a given perturbation amplitude, the seismicity-rate variations are inversely proportional to the period.

For small periods, such that $(T \ll T_\tau)$, $\tau_f(t) \neq \tau(t)$ and the seismicity rate is zero between times t_0 and t_1 within each period (Fig. A1). It is maximum at time t_1 , such that the amplitude of the variations is entirely defined by the value of the stress at t_1 . The time t_0 is the first time within the period such that the stress rate is zero. Taking the derivative of eq. (A3), this directly leads to, assuming $(T \ll T_\tau)$:

$$t_0 = \frac{T}{2\pi} \arcsin\left(\frac{T}{T_\tau}\right) \approx \frac{T}{2\pi} \frac{T}{T_\tau}, \quad (\text{A6})$$

and

$$\tau(t_0) \approx \Delta\tau \left[1 + \frac{1}{2} \left(\frac{T}{T_\tau}\right)^2\right]. \quad (\text{A7})$$

The time t_1 is such that $t_1 > t_0$ and $\tau(t_1) = \tau(t_0)$. The approximation $T \ll T_\tau$ lets us write $t_1 = T - \varepsilon$, where ε is such that $\varepsilon/T \ll 1$ and it is solution of the equation:

$$\tau(t_1) \approx \dot{\tau}_a T \left(1 - \frac{\varepsilon}{T}\right) + \Delta\tau \left[1 - \frac{1}{2} \left(2\pi \frac{\varepsilon}{T}\right)^2\right]. \quad (\text{A8})$$

Equating eqs (A7) and (A8) yields:

$$\frac{\varepsilon}{T} = \sqrt{\frac{T}{\pi T_\tau}}. \quad (\text{A9})$$

The amplitude of the variations of seismicity rate is simply $\Delta R/r = R(t_1)/r - 1 = \dot{\tau}(t_1)/\dot{\tau}_a - 1$, which finally leads to the final expression:

$$\frac{\Delta R}{r} = 2\sqrt{\pi} \sqrt{\frac{T_\tau}{T}}. \quad (\text{A10})$$

The asymptotic lines for the Coulomb response in Fig. 2 show that eqs (A5) and (A10) give good approximations of the amplitude of the variations of seismicity rate in the cases where, respectively, $T/T_\tau \geq 1$ and $T/T_\tau \ll 1$.

APPENDIX B: RESPONSE OF SEISMICITY TO HARMONIC STRESS PERTURBATIONS IN THE SRM

Based on a spring-slider system subjected to a rate-and-state friction law and a few other assumptions (see Section 3), Dieterich (1994) proposed an equation to link the seismicity rate on a fault $R(t)$ to a given stress history $\tau(t)$. Assuming a constant normal stress on the fault, his eqs (9) and (11) yield:

$$\begin{cases} a\sigma \frac{d\gamma}{dt} = 1 - \gamma(t) \frac{d\tau}{dt}, \\ \frac{R(t)}{r} = \frac{1}{\dot{\tau}_a \gamma(t)}, \end{cases} \quad (\text{B1})$$

where r is the constant seismicity rate under constant stressing rate $\dot{\tau}_a$, a is a rate-and-state constitutive parameter and σ is the effective normal stress on the fault, assumed to be constant here. Taking the origin of time and shear stress so that $\tau(0) = 0$, and supposing that $R(t=0^-) = r$, one can integrate the system of eqs (B1) to get:

$$\frac{R(t)}{r} = \frac{e^{\tau(t)/a\sigma}}{1 + \frac{1}{t_a} \int_0^t e^{\tau(x)/a\sigma} dx}, \quad (\text{B2})$$

where $t_a = a\sigma/\dot{\tau}_a$ represents the characteristic time for the evolution of the seismicity rate.

Eq. (B2) can be easily linearized and solved in the case of small harmonic variations of the shear stress:

$$\tau(t) = \dot{\tau}_a t + \Delta\tau e^{i\omega t}, \quad (\text{B3})$$

where $\omega = 2\pi/T$, and we assume that $(\Delta\tau \ll a\sigma)$ (small perturbation assumption). In this case, once the steady-state regime is established (i.e. for times such that $(t \gg t_a)$) eq. (B2) reduces to:

$$\frac{R(t)}{r} = \frac{1 + \frac{\Delta\tau}{a\sigma} e^{i\omega t}}{\frac{1}{t_a} \int_0^t e^{\frac{x-t}{t_a}} \left(1 + \frac{\Delta\tau}{a\sigma} e^{i\omega x}\right) dx}. \quad (\text{B4})$$

Simplifying eq. (B4), the seismicity rate can be written $R(t) = r + \Delta R e^{i\omega t}$ where the relative amplitude $\Delta R/r$ of the harmonic variations of seismicity rate is given by:

$$\frac{\Delta R}{r} = \frac{\Delta\tau}{a\sigma} \frac{i\omega t_a}{1 + i\omega t_a}. \quad (\text{B5})$$

Eq. (B5) suggests two regimes of response of the seismicity to small stress perturbations depending whether $\omega t_a \gg 1$ or $\omega t_a \ll 1$, that is

depending on the value of the perturbing period T compared to the critical period

$$T_a = 2\pi t_a. \quad (\text{B6})$$

For perturbations at small periods ($\omega t_a \gg 1$, or $T \ll T_a$), the seismicity rate becomes proportional to the stress perturbation,

$$\frac{\Delta R}{r} = \frac{\Delta\tau}{a\sigma}, \quad (\text{B7})$$

and the response is thus period-independent and in phase with the shear stress. For perturbations of large periods ($\omega t_a \ll 1$, or $T \gg T_a$), the seismicity rate follows the stress rate, as in the CFM:

$$\frac{\Delta R}{r} = \frac{i\omega \Delta\tau}{\dot{\tau}_a}. \quad (\text{B8})$$

This regime will be referred to as the Coulomb regime.

When the shear-stress perturbation becomes large, eq. (B2) can still be solved in the two configurations where $\omega t_a \ll 1$ and $\omega t_a \gg 1$. For a shear stress increasing at constant rate $\dot{\tau}_a$ with harmonic variations of amplitude $\Delta\tau$ and period T

$$\tau(t) = \dot{\tau}_a t + \Delta\tau \sin \omega t, \quad (\text{B9})$$

once the steady-state regime is established (i.e. for times such that $t \gg t_a$) eq. (B2) becomes:

$$\frac{R(t)}{r} = \frac{e^{\frac{\Delta\tau}{a\sigma} \sin \omega t}}{\frac{1}{t_a} \int_0^t e^{\frac{x-t}{t_a}} e^{\frac{\Delta\tau}{a\sigma} \sin \omega x} dx}. \quad (\text{B10})$$

In the case of a harmonic perturbation at short periods $\omega t_a \gg 1$ ($T \ll T_a$), the periodic term in the integral in eq. (B10) evolves much faster than the exponential term, such that the denominator in eq. (B10) can be approximated by:

$$\frac{1}{t_a} \int_0^t e^{\frac{x-t}{t_a}} e^{\frac{\Delta\tau}{a\sigma} \sin \omega x} dx \approx \langle e^{\frac{\Delta\tau}{a\sigma} \sin \omega t} \rangle \int_0^t \frac{1}{t_a} e^{\frac{x-t}{t_a}} dx \approx \langle e^{\frac{\Delta\tau}{a\sigma} \sin \omega t} \rangle, \quad (\text{B11})$$

where

$$\langle e^{\frac{\Delta\tau}{a\sigma} \sin \omega t} \rangle = \int_0^1 e^{\frac{\Delta\tau}{a\sigma} \sin 2\pi t} dt. \quad (\text{B12})$$

So, in this case, the seismicity rate can simply be written:

$$\frac{R(t)}{r} = \frac{e^{\frac{\Delta\tau}{a\sigma} \sin \omega t}}{\langle e^{\frac{\Delta\tau}{a\sigma} \sin \omega t} \rangle}. \quad (\text{B13})$$

Fig. B1(b) shows that this expression provides a good approximation of the exact solution obtained numerically. Besides, one can easily verify that eq. (B7) is simply a linear approximation of this expression when $\frac{\Delta\tau}{a\sigma} \ll 1$.

In the opposite case where $\omega t_a \ll 1$ (i.e. $T \gg T_a$), the exponential term in the integral in eq. (B10) is significantly non-zero only when the integration parameter x lies within a few t_a from t . Since $T_a \ll T$, the sine term does not vary much on this interval and can be approximated by $\sin \omega x \approx \sin \omega t + (x - t)\omega \cos \omega x$. With this approximation, and once the steady state regime has been reached

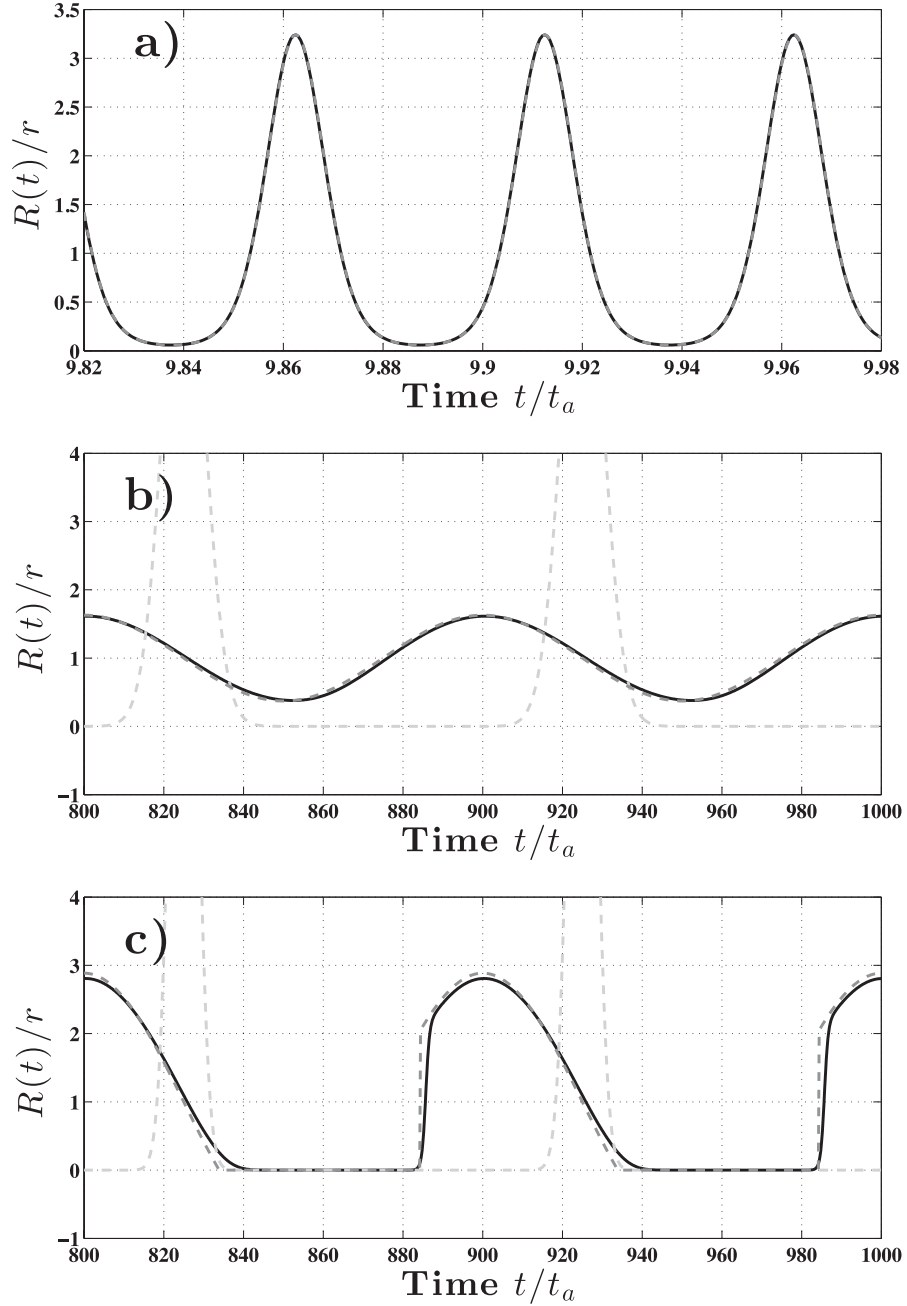


Figure B1. Evolution of the seismicity rate under a harmonic stress perturbation according to the SRM, simulated and analytical evolution. On all three plots, the plain black line shows the solution by solving eq. (B10) numerically. (a) $\beta = 2$ and $T/t_a = 5 \times 10^{-2}$ (i.e. $T \ll t_a$ case), dashed grey line plots eq. (B13). (b) $\beta = 10$ and $T/t_a = 100$ (i.e. $T \gg t_a$ case with $\beta\omega t_a \approx 0.6 < 1$), dashed dark-grey line plots eq. (B14) while dashed light-grey line plots eq. (B13) for comparison. (c) $\beta = 30$ and $T/t_a = 100$ (i.e. $T \gg t_a$ case where $\beta\omega t_a \approx 1.9 > 1$), dashed dark-grey line plots eq. (B15) while dashed light-grey line plots eq. (B13) for comparison.

(i.e. for times $t \ll t_a$), eq. (B10) reduces to:

$$\frac{R(t)}{r} = 1 + \frac{T_r}{T} \cos \omega t = \frac{\dot{\tau}(t)}{\dot{\tau}_a}, \quad (\text{B14})$$

which is analog to the Coulomb case. As in the Coulomb case, eq. (B14) is actually only valid in the case $T > T_r$ (i.e. $\frac{\Delta\tau}{a\sigma}\omega t_a < 1$), which is likely since $\omega t_a \ll 1$. However, strictly speaking, the ratio $\Delta\tau/a\sigma$ can be arbitrarily large, and thus T_r might be greater than T . This case is similar to the case examined in appendix A, and the result is the same: one simply has to replace $\tau(t)$ by its increasing

envelope $\tau_f(t)$ to get the final result. Eq. (B14) can thus be directly replaced by:

$$\frac{R(t)}{r} = \left(1 + \frac{T_r}{T} \cos \omega t\right) \mathcal{H}[\tau(t) - \tau(t_m(t))], \quad (\text{B15})$$

where $\mathcal{H}(t)$ is the Heavyside function ($\mathcal{H}(t) = 0$ for $t < 0$ and $\mathcal{H}(t) = 1$ for $t \geq 0$), and $t_m(t)$ is the time of previous shear stress maximum. Given the stress in eq. (B9), one has $t_m(t) = t - \text{mod}$

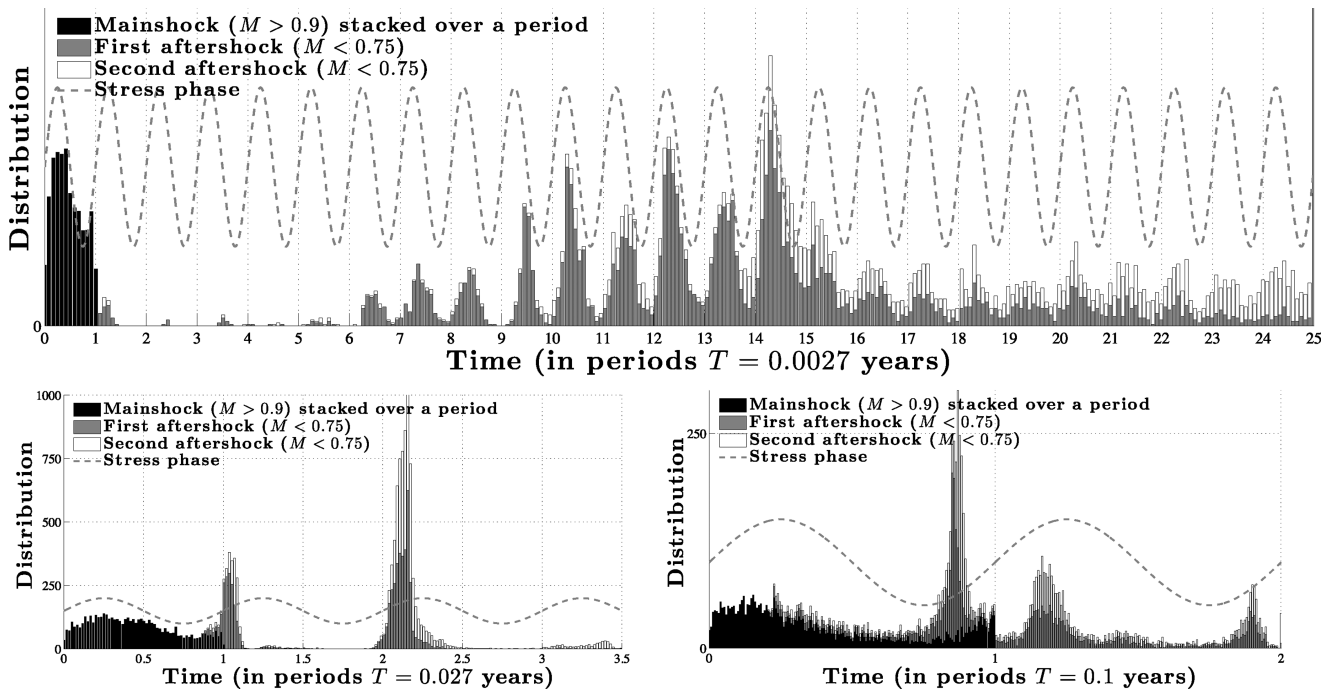


Figure C1. Timing of main shocks ($M_{\text{lin}} > 0.9$) stacked over the perturbing period ($T = 0.027$ yr) for a fault loaded at $V_{\text{pl}} = 1$ cm yr $^{-1}$, and relative timing of the first two small aftershocks ($M_{\text{lin}} < 0.75$). The time distribution of the main shocks is indicated with black bars, while the time distribution of the aftershocks is indicated with grey bars. The dashed grey sine-wave schematically shows the phase of the stress applied on the fault. The timing of aftershocks seems to be largely affected by the stress perturbation, and their phase with respect to the stress perturbation varies through time, owing to the influence of the afterslip caused by the main shock.

($t - t_0, T$), where t_0 is the time of first maximum stress within one period (same thing as in Appendix A), and is:

$$t_0 = \frac{T}{2\pi} \cos^{-1} \left(-\frac{T}{T_r} \right). \quad (\text{B16})$$

Fig. B1(c) shows that eq. (B15) provides a fairly good approximation of the exact solution.

APPENDIX C: RESPONSE OF AFTERSHOCKS TO HARMONIC STRESS PERTURBATIONS IN THE FINITE-FAULT MODEL

Events that rupture the entire seismogenic patch and have a magnitude $M_{\text{lin}} > 0.9$ are usually followed by two aftershocks. Comparing the timing of these first two aftershocks with the stress perturbation ongoing on the fault brings to light another manifestation of the inverse dependence of T_a on the loading rate. Fig. C1 shows the distribution of the timings of $M_{\text{lin}} > 0.9$ events stacked over one perturbing period and the relative timing of the first two aftershocks. Note that $M_{\text{lin}} > 0.9$ events are about the same set as the $M_{\text{lin}} > 1$ events, as the distribution of magnitudes from Fig. 8 indicates that very few events have magnitudes between 0.9 and 1. After a $M_{\text{lin}} > 0.9$ event happens, afterslip at the edge of the seismogenic patch induces the stressing rate $\dot{\tau}_a$ to suddenly increase, and then slowly decay back to its interseismic value (e.g. Perfettini & Avouac 2004). The inverse dependence of T_a on the loading rate would thus cause T_a to suddenly drop after the main shock (i.e. the $M_{\text{lin}} > 0.9$ event) and then increase back to its interseismic value.

With this expected variation of T_a in mind, the variation of the phase of aftershocks in the case of a perturbing period

$T = 2.7 \times 10^{-3}$ yr (Fig. C1, top row) can be understood. Fig. 12 (grey circles with yellow line) indicates that the phase Φ between the seismicity rate of large events and the shear stress perturbation is slightly negative, meaning that the peak of seismicity rate happens slightly after the peak of stress when no afterslip occurs. However, Fig. C1 (top row, $T = 0.0027$ yr) shows that if the main shocks have an expected slightly negative phase, the aftershocks have different phases depending on their timing relative to the main shock. Aftershocks happening within one period of the main shock have a positive phase $\Phi > 0$ (they happen before the maximum of the shear stress, almost at the maximum of shear stress rate), while the phase of aftershocks happening around 9 or 10 periods later drops to $\Phi \approx -\pi/4$ and then gradually increases to $\Phi \sim 0$ for aftershocks happening 14 or more periods after the main shock. Noting from Fig. 12 that $\Phi > 0$ corresponds to $T_a < T$, $\Phi \approx -\pi/4$ to $T_a \gtrsim T$ and $\Phi \sim 0$ to $T_a \gg T$, this variation of phase can indeed be explained by the value of T_a dropping right after the main shock and then slowly increasing, while the period T of the stress perturbation remains the same.

The case of the perturbing period $T = 0.027$ yr (Fig. C1, bottom left) displays a similar pattern. The mainshocks happen with a slightly negative phase ($T < T_a$ according to Fig. 7), and the aftershocks happen within either 1 or 2 periods of the main shock. Aftershocks happening within one period of the main shock have an almost $\pi/2$ phase (Coulomb regime, $T_a \ll T$), while the phase of the ones happening during the next period starts decreasing ($T_a \lesssim T$).

Fig. C1 also shows the case of a perturbing period $T = 0.1$ yr (bottom right), which illustrates the complexity of the seismicity on the fault. The main shocks are getting close to the Coulomb regime ($\Phi > 0$ in Fig. 12 for $T = 0.1$ yr), and so the aftershocks would tend to remain in the same regime when decreasing T_a as $\dot{\tau}_a$ increases

due to afterslip. However, in this case, the period of the perturbation becomes larger than the typical main shock–aftershock time, which is usually less than 0.05 yr, as can be seen in the cases of perturbations periods $T = 0.0027$ and 0.027 yr. As a result, when main shocks happen at the beginning of the period, which is the case for the majority of them, induced aftershocks cannot ‘wait’ an entire period to happen, and they nucleate before the end of the period as soon as the stress on the fault starts increasing again. The global shear stress reduction due to the perturbation thus still appears to prevent them from nucleating, but as soon as the perturbing stress starts increasing again, these events nucleate, resulting in a peak in the seismicity rate at the end of the period. These considerations explain the complexity that is observed in the seismicity rate in Fig. 6 for periods $T = 0.027$ and 0.1 yr: the different peaks in the seismicity rate within one period correspond to different populations of events that happen under different loading conditions, and thus with different phases. Stacking them altogether thus results in a complex seismicity rate that eq. (19) cannot fit properly. This explains why isolating large events as is done in Fig. 11, which all respond with the same phase, leads to a much more successful fit of eq. (19) to the seismicity rate.

SUPPORTING INFORMATION

Additional Supporting Information may be found in the online version of this article:

Figure S1. Slip on the fault presented in Section 4, when the fault undergoes a harmonic perturbation at period $T = 0.0027$ yr.

Figure S2. Evolution of the stress and stress rate with time in the nucleation zone, for the unperturbed fault model with the response of Fig. 4(a).

Figure S3. Evolution of the slip velocity with time in the nucleation zone, at the same locations as in Fig. S2.

Figure S4. Comparison of the frequency response of faults with creeping zones of different sizes, for large events rupturing the entire seismogenic patch.

Figure S5. Upper plot: distribution of times between the last seismic event and the applied stress step.

Figure S6. Comparison of the magnitude distribution of the seismic events produced by the seismic patch on a fault undergoing a random perturbation in time.

Figure S7. Distribution of linear magnitudes M_{lin} of seismic events that rupture the entire seismogenic patch, as a function of the length of the seismogenic patch.

Figure S8. The non-linearity of fault response to harmonic perturbations due to resonances with the return period of characteristic events happening on the fault. In these two simulations, $D_c = 1 \mu\text{m}$ and $\sigma = 1 \text{ MPa}$, similarly to the case of the red squares in Fig. 14 from the main text.

Figure S9. The increase of response of the seismogenic patch around period T_a for different properties of the rate-strengthening zone.

Figure S10. Upper plot: Stress on the fault in the seismogenic patch, with the colour corresponding to fault positions from Figs S2 and S3, for a 3-kPa-stress perturbation at $T = 0.0027$ yr (<http://gji.oxfordjournals.org/lookup/suppl/doi:10.1093/gji/ggu144/-/DC1>).

Please note: Oxford University Press is not responsible for the content or functionality of any supporting materials supplied by the authors. Any queries (other than missing material) should be directed to the corresponding author for the article.